PAPER

Check for updates

Tailoring Yb^{3+} energy levels by local configuration in the garnet structure: the case of Ca$_3$(NbGa□)$_5$O$_{12}$ laser single crystals as a model for Yb:YAG

María Dolores Serrano, [a] Concepción Cascales, [a] Carlos Zaldo, *[a]
Nicolas Trcera, [b] João Elias F. S. Rodrigues, [c] Giulio Gorni, [d]
Mamoru Kitaura [e] and Hirokazu Masai [f]

Crystallographic information on the cationic interactions that may broaden the Yb^{3+} optical bands in garnets for sustaining shorter femtosecond laser pulses is provided. It is shown that the energy of the Yb^{3+} $^2F_{7/2}(0) \leftrightarrow {}^2F_{5/2}(0')$ optical absorption ($0 \leftrightarrow 0'$ OA), measured at a cryogenic temperature (T = 6 K) in Ca$_3$(NbGa□)$_5$O$_{12}$ (CNGG)-type disordered single-crystal garnets, is sensitive to the electric charge of the cations incorporated in the 24d tetrahedral site, while it is much less sensitive to substitutions made on the 16a octahedral site. CNGG single-crystals nominally doped with 8 at% of Yb and further modified with other optically silent cations were grown by the Czochralski method. Li$^+$, Mg^{2+}, Ge^{4+}, and Ti^{4+} were successfully incorporated into the crystals. Further, Yb-doped CNGG crystals grown in the composition limits for congruent melting were studied to explore the effect of a change in the cationic vacancy density. The lattice position of the three latter cations is unequivocally determined by the combined analyses of X-ray absorption spectroscopy (XAS) and single-crystal X-ray diffraction (scXRD) refinements. Li$^+$ and Ge^{4+} exclusively fill the tetrahedral garnet site, with a strong reduction in the cationic vacancy density monitored in the Li case by positron annihilation lifetime spectroscopy (PALS). Ti^{4+} sits exclusively in the octahedral garnet site with no effect on the crystal cationic vacancy density, while Mg^{2+} is distributed in the three garnet sites with preference for the tetrahedral one and a moderate reduction in the crystal vacancy density. The Yb^{3+} $0 \leftrightarrow 0'$ OA bands observed at λ = 973 nm, 971.9 nm, 971.3 nm, 971.1 nm and 969.6 nm are correlated with the presence of a vacancy (electric charge Q = 0), Li$^+$, Mg^{2+}, Ga^{3+} and Ge^{4+} in the tetrahedral garnet sites nearest to Yb^3, respectively. However, the incorporation of Ti^{4+} in the octahedral site substituting mainly Ga^{3+} has no observable effect on the Yb^{3+} $0 \leftrightarrow 0'$ OA. The elimination of tetrahedral cationic vacancies slightly reduces the Yb^{3+} 300 K luminescence bandwidth in the Li$^+$- and Mg^{2+}-modified CNGG crystals, while the new energy levels associated with the tetrahedral Ge^{4+} compensate for this effect and slightly increase it.

1 Introduction

The generation of ultrashort laser pulses requires active media with a large optical emission bandwidth.[1] Additionally, other

[a] Instituto de Ciencia de Materiales de Madrid, Consejo Superior de Investigaciones Científicas, c/Sor Juana Inés de la Cruz 3, 28049 Madrid, Spain.
E-mail: cezaldo@icmm.csic.es
[b] Synchrotron Soleil, 91192 Gif-sur-Yvette Cedex, France
[c] Synchrotron ALBA, Carrer de la Llum 2, 26, Cerdanyola del Vallès, 08290 Barcelona, Spain
[d] Instituto de Cerámica y Vidrio. Consejo Superior de Investigaciones Científicas, c/Kelsen 5, 28049 Madrid, Spain
[e] Faculty of Science, Yamagata University, Yamagata, 990-8560, Japan
[f] Department of Materials and Chemistry, National Institute of Advanced Industrial Science and Technology (AIST), Osaka, 563-8577, Japan

favourable physical properties of the media, namely, high thermal conductivity, favourable thermo-mechanical properties and low anisotropy, are also required for efficient laser operation.

Trivalent lanthanides (Lns), with an [Xe]4f^n electronic configuration, have much smaller optical (absorption and emission) bandwidths than transition metal ions, for instance Ti^{3+} ([Ar]3d^1), because the host crystal field (CF) on the f orbitals is shielded by the outer, although less energetic, 5s and 5p orbitals of Lns. However, Lns that can be resonantly pumped with infrared semiconductor diode lasers (DL) have attracted great attention as laser centres due to the fact that they have a low energy difference between the absorbed and emitted photons (low quantum defect), and thus, the heat transferred to the host is minimised, allowing the output laser intensity to be scaled up.

In comparison to other laser Lns, the near-to-full electronic configuration of Yb^{3+}([Xe]$4f^{13}$) has the strongest interaction with the host lattice vibrations, resulting in intrinsically larger optical absorption and emission bandwidths than the other Lns. Yb^{3+} has received a lot of attention as an in-band DL pumped mode-locked laser system.[2] Although many different glasses and single crystals have been tested as Yb^{3+} hosts, the cubic $Y_3Al_5O_{12}$ (YAG) garnet remains the workhorse for industrial laser systems in most cases because it possesses the aforementioned favourable physical properties; however, the narrow laser gain bandwidth (even shorter than the fluorescence bandwidth) of Yb^{3+} in YAG, i.e. ≈ 8 nm at $\lambda = 1030$ nm, limits the laser pulse duration to ≈ 140 fs.[3]

Fig. S1a in the SI sketches the structural units of garnet lattice with the generic formula $\{A\}_3[B]_2(C)_3O_{12}$. A, B and C correspond to the 8-fold oxygen-coordinated cations at the dodecahedral ($24c$) position, 6-fold oxygen-coordinated cations in the octahedral centrosymmetric ($16a$) site, and 4-fold oxygen-coordinated cations at the tetrahedral ($24d$) site, respectively. Different cations with diverse oxidation states can occupy these sites, giving rise to a plethora of garnet compounds. In YAG, yttrium and dopant Lns fill the $24c$ site, while aluminium fills both the $16a$ and $24d$ lattice sites.

Given that the energy of the Yb^{3+} electronic levels is determined by the strength and symmetry of the CF on the Yb^{3+} site, attempts to enlarge the Yb (and other Ln) optical bandwidths in YAG indeed have been pursued by partially or fully replacing Y^{3+} and Al^{3+} with other optically-silent isovalent cations, e.g. Gd^{3+}, Lu^{3+}, Sc^{3+}, and Ga^{3+}. In this approach, changes in the CF rely on the strain of the garnet lattice due to the ionic radius mismatch ($\Delta r = (r_2 - r_1)/r_1$) between the replaced ions (r_1 for Y or Al) and the new ones introduced (r_2). Fig. S1a graphically shows the common occupancy sites as a function of the ionic radius and site coordination, and Table S1 summarises the ionic radius mismatches for common substitutions in garnets. The possible cationic environments around the $24c$ garnet site of Yb^{3+} are shown in Fig. S1b.

According to the published 300 K photoluminescence data, the most intense Yb^{3+} emission in YAG at $\lambda = 1030$ nm has a fluorescence bandwidth with a full width at half maximum of FWHM = 85 cm^{-1}.[4] If dodecahedral Y^{3+} ($r_{Y,CN=8} = 1.019$ Å) is fully replaced by isovalent Lu^{3+} ($r_{Lu,CN=8} = 0.977$ Å), the fluorescence bandwidth is reduced to FWHM = 56.2 cm^{-1},[5] which is a small change likely due to the very small Y/Lu radius mismatch, i.e. $\Delta r = -0.0412$. When the octahedral Al^{3+} ($r_{Al,CN=6} = 0.535$ Å) is replaced by Sc^{3+} ($r_{Sc,CN=6} = 0.745$ Å, i.e. $\Delta r_{Al-Sc,CN=6} = 0.392$), the fluorescence bandwidth increases up to FWHM = 127 cm^{-1}.[4] Alternatively, the full replacement of octahedral and tetrahedral Al^{3+} with Ga^{3+} leads to an emission bandwidth of only FWHM = 102 cm^{-1},[6] which could be associated with the smaller radius mismatches induced in both sites with regard to the previous case, i.e. $\Delta r_{Al-Ga,CN=6} = 0.159$ and $\Delta r_{Al-Ga,CN=4} = 0.205$. It is seen that the isovalent replacement strategy induces a limited change in the Yb^{3+} fluorescence bandwidth in YAG-like laser garnets. Thus, it is necessary to understand the physical interactions in the garnet structure to maximise the Ln optical bandwidths.

Other garnet families combine heterovalent substitutions over two sites of the garnet structure. For instance, $Ca_3Sc_2Ge_3O_{12}$ compensates the extra Ge^{4+} charge (with regard to Al^{3+}) in the tetrahedral site with Ca^{2+} charge deficit (with regard to Y^{3+}) in the dodecahedral site, basically remaining an "ordered" lattice, i.e. each $24c$, $16a$ or $24d$ garnet site is occupied by a unique A, B or C cation type. In this host, the 300 K fluorescence bandwidth of the Yb^{3+} emission at $\lambda = 1031$ nm is FWHM = 73 cm^{-1},[7] i.e. no fluorescence bandwidth enhancement with regard Yb:YAG is found.

In contrast to the above-mentioned approaches, the introduction of heterovalent substitutions, along with the concept of crystal cationic disorder, i.e. the same crystal site shared by at least two cations with different electric charges and sizes, in the $Ca_3(NbGa\square)_5O_{12}$ (CNGG, $\square$ stands for cationic vacancies) single crystal produced the largest Yb^{3+} fluorescence bandwidth reported thus far in a single crystal garnet, namely, FWHM = 220.6 cm^{-1} for the $\lambda = 1027.5$ nm emission band.[8,9]

In the CNGG single crystal (and in related compositions grown after host modification with Li^+ or Na^+ ions), Na^+, Ca^{2+} and Yb^{3+} share the dodecahedral site, while Nb^{5+} and Ga^{3+} are simultaneously distributed over the octahedral (preferential for Nb^{5+} with occupancy factor OF = 0.625) and tetrahedral (preferential for Ga^{3+}, OF = 0.821) lattice positions.[10] Furthermore, Li^+ exclusively occupies the tetrahedral position, removing cationic vacancies at this site.[11] At the local level, the cationic distribution around Yb^{3+} is random but with given probabilities from the macroscopic point of view. In this case, the CF on Yb^{3+} is determined not only by the change in the Yb–O bonding distance but also by the oxidation state of other surrounding cations, i.e., the total electric charge around Yb^{3+}. This is the ultimate reason for the large enhancement in the Yb^{3+} fluorescence bandwidth in CNGG with regard to other garnets.

The CNGG capability to incorporate foreign cations, often in excess of 10% of the corresponding site occupancy, gives the unique opportunity for the study of the influence of the cationic size and charge modification in the garnet structure in the spectroscopy of Lns. Yb^{3+} is selected in the present study because of its largest sensitivity to the lattice environment. To unambiguously determine the impact of structural changes on the optical spectroscopy of Yb^{3+}, we focused our study on the $^2F_{7/2}(0) \leftrightarrow {}^2F_{5/2}(0')$ transition (shortly $0 \leftrightarrow 0'$) monitored at low temperature ($T = 6$ K) with a high spectral resolution (<0.2 nm), which effectively eliminates the thermal effects observed in spectroscopic measurements conducted at room temperature (RT).

The purpose of the present work is to examine the effect of the incorporation in the octahedral and tetrahedral garnet sites (shortest intercationic distances with the dodecahedral site, see SI Table S3) of optically silent cations (Li^+, Mg^{2+}, Ge^{4+} and Ti^{4+}) with increasing electric charge (Q) but ionic radius not very different from that of Nb^{5+} and Ga^{3+} for each corresponding coordination; see SI Table S2. We intend to reach conclusions about how to modify the energy of the Yb^{3+} levels by a proper combination of cations, which in the end may give rise to the operation of garnet hosts, such as YAG, LuAG, and GGG, in the ultrashort (<100 fs) laser pulse duration regime.

A major uncertainty to reach conclusions in this respect is the lack of unequivocal knowledge of the site occupied by the cations used for lattice modification. To address this point, we use a combination of X-ray absorption near edge structure (XANES) and extended X-ray absorption fine structure (EXAFS) spectroscopies for Mg^{2+}, Ti^{4+}, and Ge^{4+} cations and single crystal X-ray diffraction (scXRD) analyses for all the studied crystals.

The vacancies present in the three cationic sites of the CNGG garnet provide zero electric charge ($Q = 0$) on these sites. It is known that in ≥ 5 at% Yb-doped CNGG, the dodecahedral vacancies disappear, while their density in the octahedral site is significantly reduced. Only vacancies in the tetrahedral site remain in a significant concentration after Yb doping.[10,11] Even without any experimental proof, some authors postulate than Li^+ is incorporated in the octahedral garnet site,[12] despite the fact that firm experimental evidence of the incorporation of Li^+ exclusively in the tetrahedral garnet site and strong reduction of the corresponding cationic vacancies was previously provided.[11] To get a deeper insight into the role of the different crystal modifiers on the cationic vacancy density, we now provide further evidence of their evolution by positron annihilation lifetime spectroscopy (PALS).

2 Experimental techniques

2.1. Crystal growth

Pure and modified 8 at% Yb:CNGG single crystals were grown in air using the Czochralski technique and a Cyberstar puller. Garnet powders obtained by solid-state synthesis (SSS) were melted in Pt crucibles. Details of SSS can be found in the SI, Section S2, and details of the CNGG crystal growth procedures can be found in our previous works.[10,11,13] CNGG modifications with Li, Mg, Si, Ge, Ti and V were attempted, but successful crystal growth and cationic incorporation into the garnet lattice were possible only for Li, Mg, Ge and Ti modifiers. The presence of Li in the crystal was assessed in a previous work using NMR and neutron diffraction analyses.[11] The incorporation of Yb as well as Mg, Ge and Ti modifier cations into the single-crystal garnet lattice was qualitatively confirmed by energy dispersed X-ray fluorescence (EDX) using an EDAX Genesis XM2i probe in a FEI Nova Nano SEM230 scanning electron microscope; see Fig. S7 of Section S3. Further, the content of the different elements was found directly in the crystals by X-ray fluorescence analyses (XFA) in a JEOL Superprobe JXA-8900 Electron Probe Micro Analyser (EPMA). The ZAF method[14] and corresponding elemental standards, CaO, Nb_2O_5, Ga_2O_3, Yb_2O_3, MgO, GeO_2 and TiO_2, were used. Given that the segregation coefficient (ratio between atomic crystal and melt compositions) of Yb is near to one,[11,13] for simplicity the melt crystal composition is used to name the samples. The segregation coefficients of Ge and Ti were found to be 0.4 and 0.96 assuming tetrahedral and octahedral site occupancies, respectively (see later sections).

Two 8 at% Yb:CNGG crystals with 10 at% and 20 at% Si substitution of Ga in the initial charge were grown. The transparency of these crystals was poor; see in SI Fig. S3d and EDX and EMPA analyses show that Si is incorporated in a very

small amount, with a segregation coefficient of 0.15. Further, crystal regions with a low Ga content were observed; thus, these solidified materials were not a single phase. The growth of 15 at% V-modified 8 at% Yb:CNGG produced a garnet single crystal, but EDX and EPMA analyses showed that V is not incorporated into the garnet lattice; see SI Fig. S7f.

2.2. Positron annihilation lifetime spectroscopy

Positron annihilation lifetime spectroscopy (PALS) was performed using a positron surface analyser PSA TypeL-II (Toyo Seiko Co., Ltd) adopting an anticoincidence processing system.[15] A ^{22}Na source, which was encapsulated with Kapton® film, was used for measurement. The accumulated counts for each sample was 10^7.

Positron annihilation lifetimes and relative intensities were determined using the LT9 program for decay analyses.[16] The apparatus response function (resolution function) and background signals were evaluated using stainless steel (CRM 5607-a) from the National Metrology Institute of Japan (NMIJN).

The experimental PALS spectrum $S_{ex}(t)$ is given by a convolution of the theoretical function $S(t)$ with the resolution function $R(t)$, as follows:

$$S_{ex}(t) = \int_0^\infty R(t - t_0)S(t_0)dt_0 \tag{1}$$

where t_0 is called the zero-time, which corresponds to the time at the peak-top of the $S(t)$ function. The resolution function $R(t)$ is also approximated by a weighted sum of a few Gaussian functions, as described by Kansy and Giebel.[16] In this work, the PALS spectra were analysed according to the two-state trapping model of bulk and defect states,[17] for which PALS spectra are reproduced by the function $S(t)$ given by the linear combination of two exponential decays with appropriate weights, as follows:

$$S(t) = \frac{I_1}{\tau_1}\exp\left(-\frac{t}{\tau_1}\right) + \frac{I_2}{\tau_2}\exp\left(-\frac{t}{\tau_2}\right) \tag{2}$$

where τ_1 and τ_2 ($> \tau_1$) are the positron annihilation lifetimes at the bulk and defect states and I_1 and I_2 are the corresponding relative intensities integrated over time, respectively. The value of τ_1 is influenced by positron trapping at a defect state. The bulk lifetime free from the positron trapping at the defect state, τ_B, was calculated using the following equation:

$$\tau_B = \left(\frac{I_1}{\tau_1} + \frac{I_2}{\tau_2}\right)^{-1} \tag{3}$$

The values of τ_B are compared between experiments and calculations to validate whether they were carried out appropriately.[18]

2.3. X-ray absorption spectroscopy (XAS)

XANES and EXAFS spectra of Mg and Ti were collected at the LUCIA beamline of the SOLEIL synchrotron facility,[19] with an injected electron energy and current of 2.75 GeV and 500 mA, respectively. XAS spectra were collected in fluorescence mode with a silicon drift diode detector applying a dead time correction. The bulk samples were put on graphite tape stuck on copper slides. The sample holder was rotated by 35°

(for Mg K-edge) and 5° (for Ti K-edge) to increase the signal and minimise self-absorption effects as much as possible.

Mg K-edge XAS spectra were obtained using a KTP(111) double-crystal monochromator for CNGG samples and a Multi-layer Grazing Monochromator (MGM) for Mg-model compounds. The first inflection point of the Mg K-edge of periclase MgO at 1306.6 eV was used for energy calibration of the monochromator. XAS spectra were recorded over the energy range of 1270 to 1598 eV with variable energy steps of 2 eV between 1270 and 1298 eV; 0.2 eV between 1298.2 and 1333 eV; 0.5 eV between 1333.5 and 1450 eV; 1 eV between 1451 and 1550 eV and 2 eV between 1552 and 1598 eV. In all cases, a counting time of sixteen seconds per point was used. To increase the signal-to-noise ratio, a total of 16 spectra per sample were averaged.

Ti K-edge XAS spectra were collected using an Si(111) double crystal monochromator over an energy range of 4850 to 5998 eV, with steps of 2 eV from 4850 to 4956 eV; 0.2 eV from 4956.2 to 5000 eV; 0.5 eV from 5000.5 to 5085 eV; 1 eV from 5086 to 5500 eV and 2 eV from 5502 to 5998 eV. For each point, the counting time was three seconds. Two spectra were averaged to increase the signal-to-noise ratio. Metallic titanium foil was used to calibrate the monochromator at 4966 eV for the first inflection point of the spectrum.

Ge K-edge (11.103 keV) XAS experiments were performed in transmission mode at the BL22-CLÆSS beamline of CELLS-ALBA.[20] A collimated beam with dimensions of $1(H) \times 1(V)$ mm² was used. The monochromatic beam was generated by a pair of Si(311) crystals. Finely ground powders were mixed with cellulose and pelletised into 5 mm diameter discs to achieve the optimal absorption edge jump. XAS data were collected across a k-range extending up to 14 Å⁻¹ under ambient conditions, with a step scanning of 0.3 eV for XANES and 1 eV for EXAFS.

XAS spectra were collected both for modified Yb:CNGG single crystals and for the Ge or Ti reference crystals specifically grown for this purpose; see in SI, Section S4. In all cases, the EXAFS oscillations $\chi(k)$ were processed using the Athena software,[21] which facilitated pre-edge background subtraction, edge jump normalisation, and extraction of the extended-range oscillations. Fourier transformation (FT) of the k-weighted $k^2 \cdot \chi(k)$ oscillations was performed using a Hanning-type apodization function ($\Delta k = 2$ Å⁻¹, $\Delta R = 2$ Å) in both k- and R-spaces, with Δk ranging from 2 to 9.5 Å⁻¹ and ΔR ranging from 1 to 4 Å.

2.4. X-ray diffraction (XRD)

The crystalline phases present in the SSS products and powdered single crystals were determined at RT by powder X-ray diffraction (XRD) $2\theta = 10°$–$80°$ scans using a Bruker D8 Advance instrument with Cu K$_\alpha$ radiation ($\lambda = 1.5406$ Å).

Crystal structures were determined from scXRD data collected at $T = 296(2)$ K with a Bruker Kappa Apex II diffractometer equipped with a fine-focus sealed Mo tube working at 50 kV/30 mA. K$_\alpha$ radiation ($\lambda = 0.71073$ Å) was selected using a graphite monochromator. Small prismatic single crystals cut from the grown crystals were selected to minimise the possibility of twinning. Data were corrected for absorption using the multi-scan method (SADABS). All calculations were performed

using the SHELXTL software.[22] Structure refinements of all studied crystals were performed in the cubic space group $Ia\bar{3}d$ (no 230) characteristic of this structure. These refinements included the evaluation of the cationic and vacancy distributions over available dodecahedral (24c), octahedral (16a) and tetrahedral (24d) garnet sites.

2.5. Optical spectroscopy

The OA spectra of the Yb³⁺ $0 \leftrightarrow 0'$ transition in the single crystals were determined at $T = 6$ K using an Agilent Technology spectrophotometer, model CARY5000. The samples were cooled with a closed cycle He cryostat. OA spectra were collected with a spectral bandwidth resolution better than 0.2 nm and the reported results are the average of at least twenty spectra.

The excitation and emission spectra of Yb³⁺ fluorescence were measured. For the compositions whose crystal growth was not successful, SSS powders were dispersed in KBr pellets, and their excitation spectra were collected. Two-side polished plates were used for successfully grown crystals. In all cases, excitation was performed using a chopped Spectra Physics Ti-sapphire (Tisa) laser. The average Tisa laser power was always kept below 100 mW (< 12.8 W cm⁻²) to minimise sample heating. The luminescence was dispersed by a Czerny–Turner SPEX (model 340E, $f = 34$ cm) monochromator and detected by a 77 K cooled Ge photodiode using a lock-in amplifier. The spectral resolution of the excitation spectra was determined by the Tisa laser emission bandwidth, *i.e.* 0.05 nm.

3. Experimental results

3.1. $Q = 0$: cationic vacancies in CNGG single crystals

It is worth noting that to grow CNGG single crystals from congruent melts, the composition of the precursor powder must deviate from the stoichiometric garnet composition; namely, a cation-deficient $Ca_3Nb_{(1.5+1.5x)}Ga_{(3.5-2.5x)}\square_xO_{12}$ composition with $x = 0.11$–0.14 is required. Most often, the $Ca_3Nb_{1.6875}Ga_{3.1875}O_{12}$ ($x = 0.125$) composition is used for the Czochralski crystal growth of CNGG.[23,24] To date, several works have studied the crystal cationic composition using X-ray or neutron diffraction techniques.[10,11,13,25,26] Beyond experimental uncertainties, two structural characteristics are concluded in all works, as follows: (a) Nb⁵⁺ and Ga³⁺ share the 16a and 24d garnet sites and (b) cationic vacancies are found in the three garnet sites, particularly significant in the tetrahedral 24d site (up to $\approx 8\%$ of the site population). Given that the electric neutrality of this CNGG formulation is based in the cationic/anionic balance (independently of x), these vacancies provide zero electric charge on the corresponding site.

Thus far, the evaluation of the crystal cationic vacancy composition has been indirectly obtained from the cationic composition. Alternatively, we used PALS as a direct method for monitoring the presence of crystal vacancies upon the introduction of Yb dopant and other cations used here to modify the crystalline lattice.

3.1.1. PALS results. To clarify the effect of impurity doping on CNGG cationic vacancies, the PALS spectra were fit with

eqn (1) and (2). Fig. 1 shows the PALS spectra of CNGG, Yb:CNGG, CLNGG, and Yb:CLNGG. Table 1 summarises the τ_i and I_i (i = 1, 2) fit values, along with those obtained for Ti- or Mg-modified 8 at% Yb:CNGG. Within the uncertainties, the τ_B values obtained are identical. These values are very close to that of other multicomponent isostructural garnets previously studied, *i.e.* $Y_3Al_5O_{12}$ (YAG, τ_B = 150–166 ps),[27] $Lu_3Al_5O_{12}$ (LuAG, τ_B = 162 ± 2 ps)[18] or $Gd_3Al_2Ga_3O_{12}$ (GAGG, τ_B = 171 ± 9 ps).[28] This fact supports the validity of our present experiments and analyses.

The PALS spectrum of CNGG can be fit with a single exponential decay function in eqn (2), while that of any other CNGG crystal studied here requires the sum of two exponential decay functions. The slow decay component of Li-modified CNGG (CLNGG) is regarded as having the same origin as the decay component of CNGG because their lifetimes are close to each other. The lifetime values determined are consistent with the calculated positron annihilation lifetimes either at the 16a or 24d garnet sites in LuAG.[18] This fact indicates that in undoped CNGG, positrons predominantly annihilate at these vacant sites, but in CLNGG, the intensity of the slow decay component is weakened by the occurrence of a fast decay component, suggesting that Li⁺ doping reduces the cation vacancy density at these sites.

To verify the effect of Li⁺ doping on the suppression of these cation vacancies in Yb-doped CNGG, the PALS spectra of 8 at% Yb:CNGG and 8 at% Yb:CLNGG are compared. The PALS spectra of these materials are also composed of two exponential decay functions, as shown in Table 1. The τ_2 values of Yb:CNGG and Yb:CLNGG are similar. Thus, it seems likely that positrons are trapped at the same cation vacancies as in CNGG and CLNGG. The I_2 value decreases in Yb:CLNGG compared to Yb:CNGG. This feature was also seen in the comparison of CNGG and CLNGG, indicating that Li⁺ doping always plays an active role in removing cation vacancies in CNGG.

It may be noted that Yb^{3+} doping of CNGG also reduces the I_2 value. The possibility that this situation could be associated with the Yb^{3+} antisite in the 16a octahedral positions, as found for other garnet constituents (Fe, Ga, Y, Gd or Er),[29] seems unlikely in the CNGG case. In fact, this Yb^{3+} antisite in the octahedral 16a site has been evidenced by the presence of dipolar magnetic optical transitions in 0.3 at% Yb:CNGG crystals[30] but the Yb solubility limit in the octahedral site is very low, $\approx 5 \times 10^{18}$ cm⁻³, and it cannot account for the strong I_2 reduction observed.

Further, the effect of Mg^{2+} and Ti^{4+} codoping on the 16a and 24d cation vacancies of CNGG was monitored by PALS. The
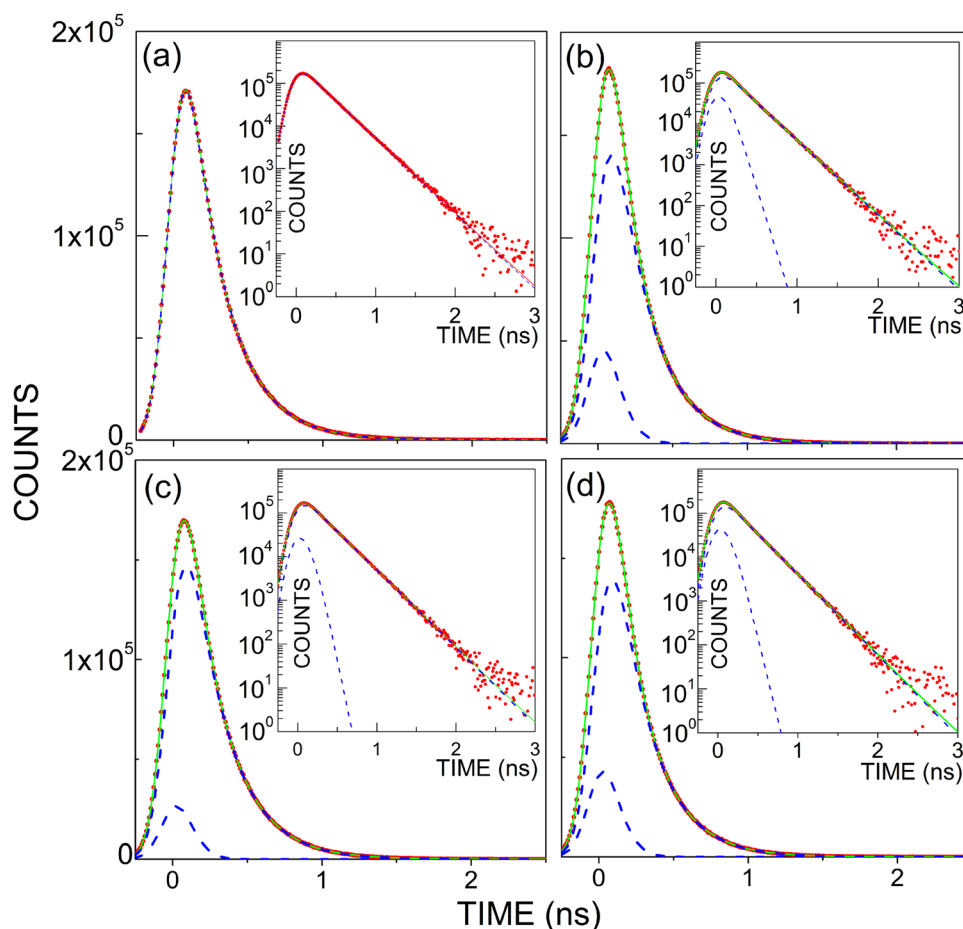

Fig. 1 Room temperature PALS spectra of (a) CNGG, (b) CLNGG, (c) 8 at% Yb:CNGG, and (d) 8 at% Yb:CLNGG. Red solid circles are the experimental data. Blue dashed lines are the components used to fit the experimental data using the two-state trapping model given by eqn (2). The sum of the blue dashed lines is indicated by a green solid line. The insets show the same results in a semilogarithmic representation.

**Table 1** PALS results for CNGG single crystals with several dopants, Yb, Li, Mg or Ti

Crystal	τ_1 (ps)	I_1 (%)	τ_2 (ps)	I_2 (%)	τ_B (ps)
CNGG	—	—	246 ± 1	100	—
8 at% Yb:CNGG	50.5 ± 0.7	9.4 ± 1.2	246 ± 1	90.6 ± 1.2	180 ± 11
10 at% Ti:8 at% Yb:CNGG	58.8 ± 9.3	11.1 ± 1.3	246 ± 1	88.9 ± 1.3	182 ± 12
30 at% Mg:8 at% Yb:CNGG	67.0 ± 10.0	13.9 ± 1.1	249 ± 1	86.1 ± 1.1	181 ± 12
CLNGG	67.8 ± 4.9	16.6 ± 0.7	237 ± 1	83.4 ± 0.7	167 ± 6
8 at% Yb:CLNGG	59.0 ± 7.0	15.6 ± 1.1	236 ± 1	84.4 ± 1.1	160 ± 9

value of I_2 in 8 at% Yb:CNGG decreases upon Mg^{2+} codoping, as in the case of Li^+ codoping. However, Mg^{2+} codoping is not as effective as Li^+ in reducing the 16a or 24d cationic vacancies because, as will be shown later, Mg^{2+} is distributed in the three garnet lattice sites. Conversely, the value of I_2 in 8 at% Yb:CNGG is not changed by Ti^{4+} codoping. Clearly, the incorporation of Ti^{4+} into Yb:CNGG has little effect on cation vacancies at 16a and 24d sites.

Based on the PALS experiments alone, it is difficult to identify which cationic vacancies are removed by the incorporation of Yb^{3+}, Li^+, Mg^{2+}, or Ti^{4+} into CNGG. In fact, the τ_2 values calculated using a two-component density functional theory for LuAG are close each other, i.e. 274 ps, 239 ps and 233 ps for 24c, 16a and 24d, respectively.[18] To get a clearer picture of the crystallographic changes induced by these cationic incorporations, we present the XAS and scXRD results in following sections.

3.1.2. OA of Yb^{3+} in non-modified CNGG. Fig. 2a shows a general view of the Yb^{3+} OA at T = 300 K and at cryogenic temperature (T = 6 K). The origin of these bands was discussed by Pappalardo et al. in Yb:$Y_3Ga_5O_{12}$ using a noncubic CF associated with the distortion of the oxygen cube around the 24c site.[31] These bands arise from electronic transitions between the Stark (m_J) components of the ground $^2F_{7/2}$ (0, 1, 2, 3) and excited $^2F_{5/2}$ (0′, 1′, 2′) Yb^{3+} multiplets. At both temperatures, the $^2F_{7/2}$ (0) → $^2F_{5/2}$ (0′) (shortly 0 → 0′) transition is observed near λ = 971.1 nm as the narrowest and most intense band. The bands at shorter wavelengths (higher energy) correspond to transitions from the ground energy level $^2F_{7/2}$ (0) to the excited $^2F_{5/2}$ (1′, 2′) ones. Thus, two further bands are expected in the region of 900–950 nm. Instead, at least three well-resolved bands are observed even at T = 6 K due to the not yet fully understood lattice phonon couplings of these transitions.

Other bands at longer wavelengths (lower energy) than that of the 0 ↔ 0′ one are observed at T = 300 K, for λ > 975 nm. These bands completely disappear by lowering the sample temperature to 6 K, and thus they are ascribed to transitions from the excited Stark m_J sublevels of the ground $^2F_{7/2}$ multiplet, which are populated due to the Boltzmann electronic distribution, i.e., $^2F_{7/2}$ (1, 2, 3) → $^2F_{5/2}$ (m_J) transitions. Their spectral overlap with the 0 → 0′ OA band at T = 300 K compromises the proper resolution of the features associated with the inhomogeneous broadening in the disordered CNGG lattice, i.e. different lattice environments around Yb^{3+}. Owing to this reason, spectroscopy at T = 6 K is required to disclose the effects of this disorder.
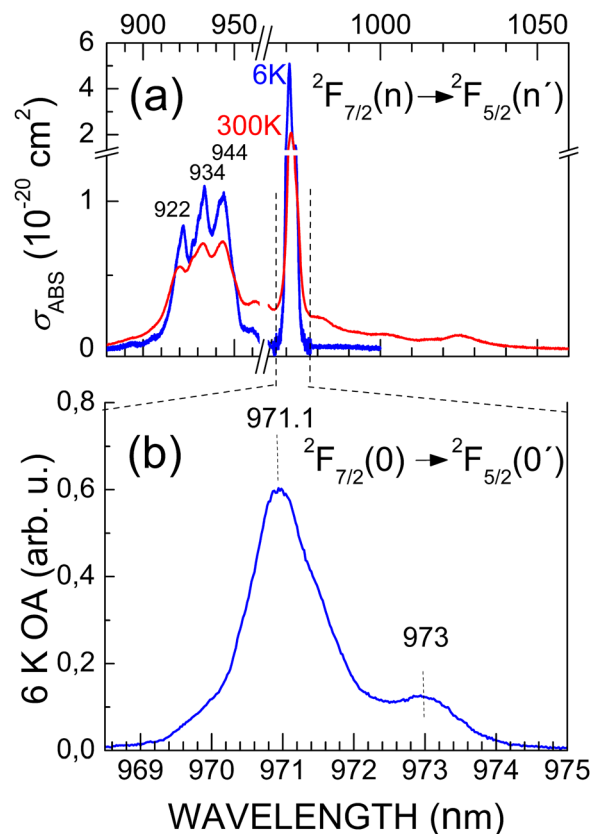
Fig. 2 Optical absorption (OA) of Yb^{3+} in the 8 at% Yb:CNGG single crystal taken at a spectral resolution of 0.2 nm. (a) General view of the absorption cross section (σ_{ABS}) at T = 300 K (red line) and at T = 6 K (blue line). (b) Expanded view of the 0 → 0′ Yb^{3+} OA measured at T = 6 K and normalised to unit area.

Fig. 2b shows the OA of Yb^{3+} in CNGG measured at T = 6 K exclusively for the 0 → 0′ transition region. It shows several contributions ascribed to different Yb^{3+} environments, whose assignment is the purpose of the present work. The most intense band at λ = 971.1 nm should correspond to 24c Yb^{3+} in the most abundant garnet lattice environment, i.e. with 24c Ca (× 4), 16a Nb (× 4) and 24d Ga (× 4 + 2) occupancies, see in SI Fig. S1b and Table S2, while the side band at λ = 973 nm reveals the presence of some lattice modification in the Yb^{3+} environment. It is worth noting that the relative intensity of the λ = 973 nm band has a tendency to increase as the crystal grows, i.e. its intensity is generally found to be higher at the final part of the crystal than in its initial part, as shown in Fig. S13b. This behaviour could be induced by the loss of gallium with crystal growth, as evidenced in Fig. S12a. This Ga loss also suggests a

slight increase in the 24d tetrahedral vacancy density given that Ga is the most abundant cation in this site and the relative enrichment in Nb^{5+} must be compensated to maintain charge neutrality.

3.2. Q = +1: Li^+-modified Yb:CNGG single crystal

Li-modified CNGG crystals (CLNGG) have been grown from melts with the composition $Ca_3Nb_{1.775}Ga_{2.95}Li_{0.275}\square_{0.025}O_{12}$, *i.e.* closer to the stoichiometric garnet formula than in the congruent CNGG case. According to the previously published combined NMR, neutron diffraction, and scXRD analysis, it was concluded that Li enters exclusively in the 24d tetragonal garnet site and that the vacancy density in this site decreases strongly upon the incorporation of Li.[11] The PALS results, as described in Table 1, also show that the incorporation of Li is the most effective way to reduce the presence of cationic vacancies remaining in CNGG after 8 at% Yb doping.

Fig. 3a shows a comparison between the $0 \rightarrow 0'$ OA of Yb^{3+} measured at $T = 6$ K in CNGG and in CLNGG. The most significant difference between these two spectra is the drastic reduction in the intensity of the $\lambda = 973$ nm OA band upon the

Fig. 3 Comparison of the $0 \rightarrow 0'$ Yb^{3+} optical absorption (OA) measured at $T = 6$ K and normalised to unit area in 8 at% Yb:CNGG (black lines) and in cationic-modified 8 at% Yb:CNGG single crystals (red lines). Spectra collected at a spectral resolution of 0.15 nm. (a) Li-modified 8 at% Yb:CNGG. (b) 30 at% Mg-modified 8 at% Yb:CNGG. (c) 20 at% Ge-modified 8 at% Yb:CNGG. (d) 10 at% Ti-modified 8 at% Yb:CNGG.

incorporation of Li^+. Further, a band that is not fully resolved appears as a shoulder at $\lambda \approx 971.9$ nm.

Considering that the cationic vacancies on the 24c site are removed by the substitution of Ca^{2+} by Yb^{3+} (thus they are not present in 8 at% Yb:CNGG) and that cationic vacancies in the 16a site are near zero in all cases,[10,11] as also shown in Table 3, the main effect of Li incorporation is the reduction of the tetrahedral 24d vacancy concentration from the OF ≈ 0.075 in 5–15 at% Yb:CNGG to only OF = 0.009 in 8 at% Yb:CLNGG, which is further confirmed by the presented PALS results. Thus, we tentatively correlate both facts and ascribe the Yb^{3+} OA band at $\lambda = 973$ nm to the specific CF created by a Yb surrounding configuration containing a 24d tetrahedral vacancy $\square_{TET}$, *i.e.* Q = 0, as the first cationic neighbour. In the same manner, the new shoulder at $\lambda \approx 971.9$ nm could be ascribed to a CF including a nearest 24d tetrahedral Li^+, Q = 1, close to Yb^{3+}.

3.3. Q = +2: Mg^{2+}-modified 8 at% Yb:CNGG single crystals

Garnets with stoichiometric concentrations of magnesium in dodecahedral, $\{Mg_3\}[Al_2](Si_3)O_{12}$ (pyrope), octahedral, $\{Gd_3\}[Mg_2](GaGe_2)O_{12}$, $\{Ca_3\}[TiMg](Ge_3)O_{12}$, $\{Ca_3\}[ZrMg](Ge_3)O_{12}$, $\{Y_3\}[MgAl](Al_2Si)O_{12}$ or distributed in both positions, $\{MgGd_2\}[Mg_2](Ge_3)O_{12}$, have been reported in the literature.[32,33] The low electronic density of Mg^{2+} makes the analysis of its crystalline lattice distribution quite unreliable using exclusively X-ray diffraction measurements. Owing to this reason, we first analyse the XAS of Mg-modified CNGG crystals to determine the garnet sites occupied by Mg and later we refine the scXRD results.

3.3.1. XAS of Mg in 8 at% Yb:CNGG single crystals. Fig. 4a shows a comparison of the Mg K-edge XANES spectrum of the 30 at% Mg-modified 8 at% Yb:CNGG crystal and of some oxides where Mg^{2+} has different oxygen coordination numbers (CN), namely, CN = 8 in pyrope ($Mg_3Al_2Si_3O_{12}$, a silicate garnet where Mg is in the 24c dodecahedral site), CN = 6 in diopside ($CaMgSi_2O_6$) and CN = 4 in the spinel ($MgAl_2O_4$).[34]

The Mg K-edge XANES is usually described by three main features in the energy range of 1305–1320 eV labelled with increasing energy as A, B and C, followed by broader and weaker peaks between ≈ 1323 and ≈ 1331 eV, labelled as D. Also, a very weak pre-edge peak labelled P is seen for the Mg CN = 8. The position of peaks A, B and C shifts towards a higher energy when the Mg CN increases. This has been used in previous works as a fingerprint of Mg coordination.[35,36]

The distinctive feature of the Mg K-edge XANES spectra in CNGG is that it simultaneously displays the characteristics of the three Mg coordinations. At least eight XANES peaks can be observed. The most intense A and C peaks of the spinel (Mg CN = 4) can be observed in CNGG at 1306.4 and ≈ 1318 eV, respectively. The intense B and C peaks of the diopside (Mg CN = 6) correspond to those observed in CNGG at 1313 and ≈ 1318 eV, respectively, with the latter being broader than in the reference due to the overlap of the CN = 4 and 6 oxygen coordinations. Finally, the A and B features of pyrope are also observed in CNGG at 1310 and 1313 eV, respectively.

Fig. 4b shows the normalised and weighted $k^2\chi(k)$ experimental EXAFS spectrum of Mg K-edge in a 30 at% Mg-modified
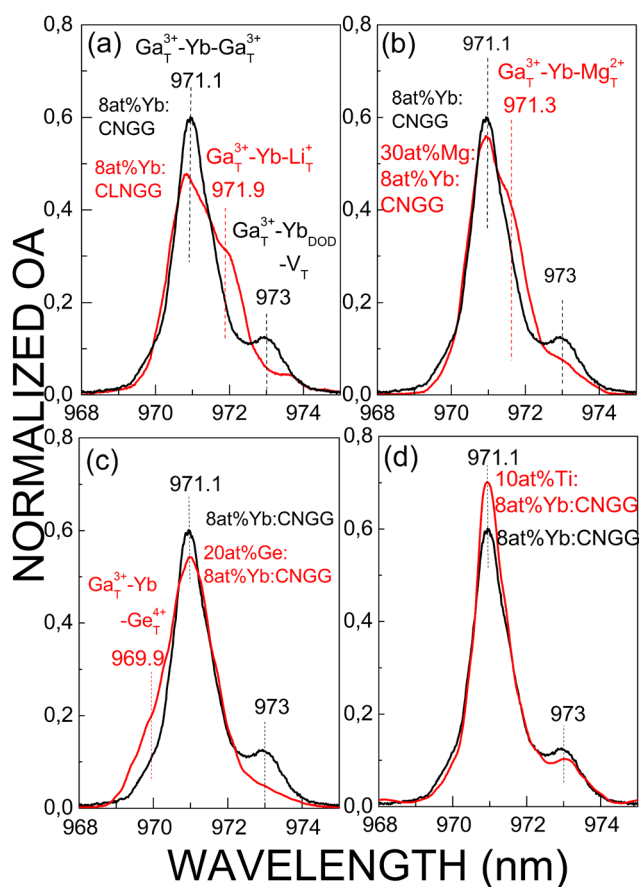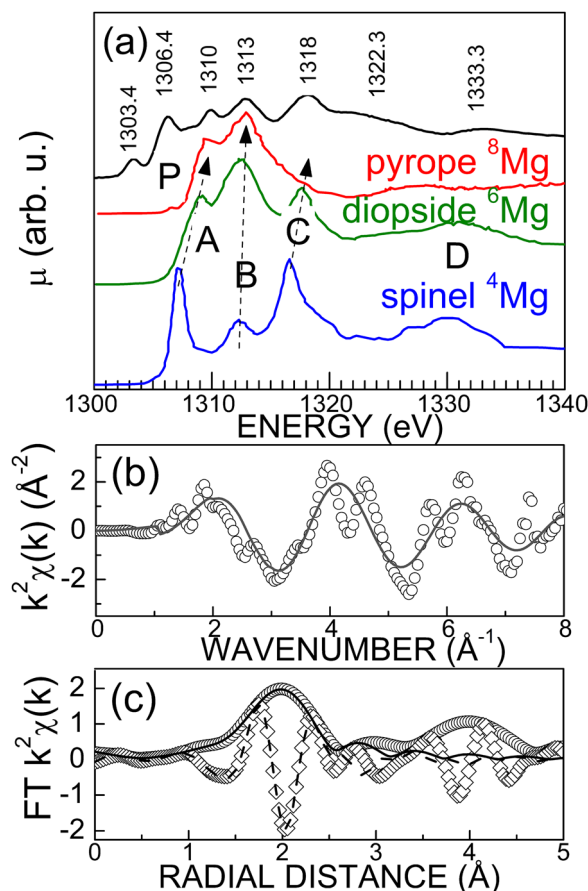
Fig. 4 Analysis of the K-edge Mg XAS of the 30 at% Mg-modified 8 at% Yb:CNGG crystal. (a) Comparison with the XANES spectra (μ) of several Mg compounds with increasing oxygen coordination number, *i.e.* ^{4}Mg, 4-fold coordinated in spinel (MgAl$_2$O$_4$). ^{6}Mg, 6-fold coordinated in diopside (CaMgSi$_2$O$_6$). ^{8}Mg, 8-fold coordination in pyrope (Mg$_3$Al$_2$Si$_3$O$_{12}$). Plots are vertically shifted for clarity. (b) $k^2 \cdot \chi(k)$ weighted EXAFS experimental spectrum (circles) and its fit (line). (c) Real (circles and continuous line) and imaginary (diamonds and dashed line) parts of the Fourier transform (FT) of the $k^2 \chi(k)$ signal in the phase-shifted scale.

8 at% Yb:CNGG crystal, and Fig. 4c shows its Fourier transform. The EXAFS fit was performed in the three possible cationic garnet sites by fixing CN = 4, 6 or 8 coordinations and leaving the Debye–Waller factors, σ^2, free, as shown in SI Fig. S11. Although in all coordinations, the observed Mg–O bond length results are 1.92–1.93 Å, the fit obtained for CN = 6 or 8 provides $\sigma^2 > 10^{-2}$ Å^2, which is unrealistic for crystal oxides, and the fit errors are significantly larger for CN = 6 and 8 than in the CN = 4 case; see SI, Table S3. Further, the Mg–O bond length determined in CNGG is consistent with the typical Mg–O distance found in CN = 4 coordination in the MgAl$_2$O$_4$ spinel,[36,37] or in akermanite, Ca$_2$MgSi$_2$O$_7$,[38] *i.e.* 1.92 Å. In contrast, the Mg–O distances found for CN = 6 in diopside (Mg–O$_4$ at 2.073 Å plus Mg–O$_2$ at 2.147 Å)[34,36,39] or for CN = 8 in pyrope (Mg–O$_4$ 2.198 Å plus Mg–O$_4$ 2.343 Å),[34,36] are clearly larger.

Therefore, the combined XANES and EXAFS analyses clearly indicate a Mg^{2+} distribution in the three garnet sites, with the majority in the 24d tetrahedral site with an Mg–O bond length

of 1.93(2) Å in the latter. Table S4 summarises the results of the EXAFS fit.

3.3.2. scXRD of Mg-modified 8 at% Yb:CNGG single crystals. According to the conclusions of the above-mentioned XAS results, the scXRD data have been refined considering the Mg^{2+} distributed over the three cationic garnet sites. The full results of this refinement can be found in Table 2 and in the SI, Section SI.6, Table S7.

Firstly, it can be mentioned that the lattice parameter determined for the 30 at% Mg-modified 8 at% Yb:CNGG crystal is $a = 12.4892$ Å, *i.e.* larger than that corresponding to its Yb doping level, $a = 12.4728$ Å for 8 at% Yb:CNGG, but lower than in undoped CNGG, $a = 12.4969$ Å, as shown in SI Table S2. This suggests the incorporation of Mg in the garnet sites with a positive radius mismatch, *i.e.* 16a and 24d, as shown in SI Table S1.

The scXRD refinement provides the OF of Mg in the three garnet sites; see Table 3 and in SI Table S7. 75% of the total Mg is incorporated in the 24d site, where a positive radius mismatch $\Delta r = +21.27\%$ occurs, which is in qualitative agreement with the lattice parameter enlargement observed with respect to 8 at% Yb:CNGG, and thus it is not surprising that the EXAFS-derived Mg–O bond distance was larger than that expected from an 8 at% Yb:CNGG lattice. The rest of Mg is distributed 17% in the 24c site with $\Delta r = -20.54\%$ and 8% in the 16a site with $\Delta r = +12.5\%$, partially counterbalancing the lattice distortions and limiting the lattice parameter increase.

3.3.3. OA of Yb^{3+} in Mg-modified 8 at% Yb:CNGG. Fig. 3b shows a comparison between the OA of Yb^{3+} measured at $T = 6$ K in 30 at% Mg-modified 8 at% Yb:CNGG and in 8 at% Yb:CNGG. The OA intensity of the $\lambda = 973$ nm band, which is assigned to Yb^{3+} near a 24d tetrahedral vacancy, decreases but not as much as in the previous Li-modified 8 at% Yb:CNGG case. Further, a shoulder appears at $\lambda = 971.3$ nm. The latter resembles that observed in the Li-modified CLNGG case, but the new OA band appears at a higher energy. Following the above-mentioned assignments, this new OA band is assigned to a Yb^{3+} ion neighbouring a 24d Mg^{2+} cation. This assignment is consistent with the large Mg population determined by the scXRD refinement for the 24d garnet site. Further, the relatively weak decrease in intensity observed for the $\lambda = 973$ nm band is also consistent with the moderate reduction of the 24d cationic vacancy density upon the incorporation of Mg, as shown in Table 3, and with the PALS results in Table 1.

3.4. $Q = 3+$: Ga^{3+} in Yb:CNGG. In CNGG, 77% of the total Ga^{3+} sits in the 24d tetrahedral garnet site, while only 23% is at the 16a octahedral one,[10] as also shown in Table 3. The most intense OA band of Yb^{3+} in CNGG peaks at $\lambda = 971.1$ nm. This band position remains unchanged for all the CNGG crystals studied independently of other cationic modifications; thus, it should correspond to the most abundant crystalline environment around Yb^{3+}, which, as explained above (Section 3.1.2), is a $Q = 3+$ (Ga^{3+}) electric charge in the 24d tetrahedral site nearby Yb^{3+}.

3.5. $Q = 4+$: Ge^{4+}- or Ti^{4+}-modified 8 at% Yb:CNGG single crystals. Natural Si-based garnets are well known in jewellery, but they only melt congruently at high pressure (> 40 kbar).[40,41] Nevertheless, the synthesis and growth of 8 at% Yb:CNGG

Journal of Materials Chemistry C

Table 2 Crystal data and structure refinement for the 30 at% Mg-modified 8 at% Yb:CNGG crystal, $\{Ca_{2.70}Yb_{0.18}Mg_{0.12}\}[Nb_{1.05}Ga_{0.89}Mg_{0.06}]$-$(Ga_{2.07}Nb_{0.22}Mg_{0.54}\square_{0.18})O_{12}$; 20 at% Ge-modified 8 at% Yb:CNGG crystal, $\{Ca_{2.733}Yb_{0.267}\}[Nb_{1.21}Ga_{0.79}](Ga_{2.34}Nb_{0.039}Ge_{0.54}\square_{0.081})O_{12}$; and 10 at% Ti-modified 8 at% Yb:CNGG, $\{Ca_{2.81}Yb_{0.19}\}[Nb_{1.58}Ga_{0.23}Ti_{0.18}](Ga_{2.75}Nb_{0.07}\square_{0.18})O_{12}$. Bond lengths and angles are given in provided CIF data. CCDC accession codes 2448685 (Mg), 2448696 (Ge) and 2448697 (Ti).

	30 at% Mg[a]	20 at% Ge[b]	10 at% Ti[c]
Temperature (K)	296(2)		
Wavelength (Å)	0.71073		
Crystal system/space group	Cubic/$Ia\bar{3}d$		
Unit cell dimensions			
$a = b = c$ (Å)	12.4892(3)	12.4165(2)	12.4720(3)
$\alpha = \beta = \gamma$ (°)	90		
Volume (Å^3)/$Z = 8$	1948.07(5)	1914.25(9)	1940.03(9)
Calculated density (Mg m^{-3})	4.584	5.004	4.852
Absorption coefficient (mm^{-1})	12.770	15.929	13.618
Crystal size (mm^3)	$0.116 \times 0.076 \times 0.052$	$0.147 \times 0.104 \times 0.04$	$0.16 \times 0.04 \times 0.03$
θ range for data collection (°)	4.00–30.49	4.02–28.28	4.02–28.2
Index ranges	$-17 \leq h, k, l \leq 17$	$-16 \leq h, k, l \leq 16$	$-16 \leq h, k, l \leq 16$
Reflections collected	69 857	54 992	54 871
Independent reflections [R(int)]	254 [0.0878]	205 [0.0427]	207 [0.0489]
Completeness to $\theta = 28.28°$	100.0%		
Refinement method	Full-matrix least-squares on F^2		
Data/restraints/parameters	254/3/27	205/2/23	205/2/23
Goodness-of-fit on F^2	1.063	1.404	1.257
Final R indices [$I > 2\sigma(I)$]			
R_1	0.0151	0.0104	0.0131
wR_2	0.0365	0.0283	0.0456
R indices (all data)			
R_1	0.0242	0.0118	0.0135
wR_2	0.0453	0.0289	0.0460
Extinction coefficient	0.0018(1)	0.00132(6)	0.0055(2)
Largest diff. peak/hole (e Å^{-3})	0.329/−0.390	0.187/−0.192	0.359/−0.449

[a] A total of 6300 frames were collected. The total exposure time was 3.5 h. The final cell constant a = 12.4892(3) Å was based on the refinement of the xyz-centroids of 4943 reflections with $I > 20\sigma(I)$ for $9.232° < 2\theta < 59.91°$. [b] A total of 5507 frames were collected. The total exposure time was 7.65 h. The final cell constant a = 12.4159(3) Å was based on the refinement of the xyz-centroids of 9252 reflections with $I > 20\sigma(I)$ for $8.040° < 2\theta < 56.35°$. [c] A total of 5507 frames were collected. The total exposure time was 7.65 h. The final cell constant a = 12.4720(3) Å was based on the refinement of the xyz-centroids of 9891 reflections with $I > 20\sigma(I)$ for $8.004° < 2\theta < 56.525°$.

Table 3 Comparison of the occupancy factors (OF) over the 24c, 16a and 24d sites in disordered CNGG crystal garnets with different Yb concentrations and cationic modifiers, Li, Mg, Ge and Ti. $\square$ stands for cationic vacancies

CNGG crystal composition			OF										
In melt (at%)	In crystal[a] (at%)		24c dodecahedral site			16a octahedral site			24d tetrahedral site				
	Yb		Ca	Yb	$\square_{DOD}$	Nb1	Ga1	$\square_{OCT}$	Ga2	Nb2			$\square_{TET}$
Undoped CNGG			0.985		0.015	0.625	0.372	0.003	0.821	0.102			0.077
8 at% Yb:CNGG	9.1		0.939	0.058	0.003	0.580	0.420		0.905	0.020			0.075
11.6 at% Yb:CNGG	12.7		0.900	0.100		0.579	0.421		0.877	0.048			0.075
15 at% Yb:CNGG	18.8		0.838	0.157	0.005	0.627	0.371	0.002	0.921	0.005			0.074
											Li		
CLNGG			0.998		0.002	0.66	0.34		0.842	0.052	0.080		0.026
8 at% Yb:CLNGG	7.57		0.931	0.069		0.67	0.33		0.810	0.069	0.111		0.009
		Mg[c]			Mg			Mg			Mg		
30 at% Mg[b]:8 at% Yb:CNGG	7	5.8	0.900	0.060	0.041	0.524	0.44	0.03	0.006	0.689	0.07	0.18	0.061
		Ge[d]									Ge		
20 at% Ge[d]:8 at% Yb:CNGG	12.8	7	0.911	0.089		0.605	0.395		0.78	0.013	0.18		0.027
		Ti[g]						Ti					
10 at% Ti[e]:8 at% Yb:CNGG	9[f]	10	0.936	0.064		0.79	0.12	0.092	0.917	0.023			0.060

[a] EPMA results. [b] In addition to the Nb amount. [c] With respect to the total cationic positions (Ca + Yb + Nb + Ga + Mg). [d] With respect to the total amount of Nb, Ga and Ge. The measured Ge concentration changes from 6 at% to 8 at% during crystal growth, and the given value is the average. [e] With respect to the total amount of Nb and Ti. [f] The measured Yb concentration changes from 8 at% to 10 at% during crystal growth, and the given value is the average. [g] With respect to the 16a site occupancy. Data are very similar to (e) hypothesis because Ti and most of Nb are in the 16a site. The measured Ti concentration changes from 9.3 at% to 11 at% during crystal growth, and the given value is the average.

crystals modified with Si^{4+} was attempted in the present work. The powders obtained by SSS were not a single phase, and the crystals (5, 10 or 20 at% Si-modified 8 at% Yb:CNGG) grown from these powders had poor optical quality, as shown in Fig. S3d. EDX and EPMA measurements show that Si was incorporated into the solid phase in small amounts, as shown in SI,

Fig. S7e, while Ga was absent in some crystal areas. All the grown Si-modified CNGG crystals show the same Yb^{3+} cryogenic (T = 6 K) OA spectrum as that of Yb:CNGG, consistent with the residual incorporation of Si into the garnet lattice. Thus, Ge^{4+} and Ti^{4+} were studied as alternative tetravalent heterovalent substitutions of Ga^{3+} or Nb^{5+}.

3.5.1. Ge^{4+}-modified 8 at% Yb:CNGG. The crystallisation of garnets containing Ge was extensively reported by Mills using different molten fluxes,[42] and an overview of the possible garnet compositions and ion site preferences was given by Geller.[32] Garnets with 4-coordinated Ge in the $24d$ tetrahedral site occur when the $24c$ site is occupied by a cation with a large ionic radius, typically Ca^{2+} or other divalent cations. Examples of these garnets are $Ca_3B_2Ge_3O_{12}$ (B = Sc, Ga, Y, Mg),[43–45] Lu_2CaMg_2-$(SiGe)_3O_{12}$,[46] $Ca_3MgBGe_3O_{12}$ (B = Zr, Sn),[47] $Ce_2CaMg_2Ge_3O_{12}$,[48] or $Ba_{0.25}Mg_{2.75}Y_2Ge_3O_{12}$.[49]

In the present study, we grew 20 at% Ge-modified 8 at% Yb:CNGG single crystals. The composition of the powder prepared by SSS was $Ca_{2.76}Yb_{0.24}Nb_{1.0883}Ga_{2.8834}Ge_{0.9833}O_{12}$, *i.e.* the incorporation of Ge was equally subtracted from the Nb and Ga compositions to avoid predetermining a specific site occupancy.

3.5.1.a. XAS of Ge in CNGG. A $Ca_3Ga_2Ge_3O_{12}$ (CGGG) garnet single crystal was also grown *via* the Czochralski method, as shown in SI Section S4.1, and a powdered CGGG single crystal was used as a reference for the XAS of Ge-modified 8 at% Yb:CNGG, as shown in Fig. 5. Fig. 5a shows similar XANES spectra for both compounds. Fig. 5b shows the Ge K-edge $k^2 \cdot \chi(k)$ weighted EXAFS oscillations, and Fig. 5c shows their Fourier transforms.

The EXAFS standard equation was used for fitting, where the theoretical scattering paths for the garnet-type $Ca_3Ga_2Ge_3O_{12}$ within the space group $Ia\bar{3}d$ were calculated using the FEFF software.[50] EXAFS analyses were performed considering the most relevant single scattering paths to describe the radial distance in the range of 1–4.0 Å. The first shell is comprised of the Ge–O1 tetrahedral site, the second shell has the Ge–Ca scattering path (CN = 2), the third shell is made of Ge–Ga with CN = 4 and the last shell is made of both Ge–Ga and Ge–Ca at a similar distance and with CN = 4. The introduction of the Ge–Ca shell is necessary to reproduce the signal at long distances. Indeed, the removal of the Ge–Ca path gave a negative σ^2 value for the Ge–Ga shell, indicating the need for an additional signal. It is important to remember that the assignment of the scatterer, especially in the case of Ga and Ge, was made according to the CIF file of the reference compound because Ge–O and Ge–Ga scatterers cannot be distinguished from EXAFS. The fit of the EXAFS spectra at the Ge K-edge of the CGGG reference shows the local structure of Ge^{4+} in the garnet, where Ge^{4+} ions are surrounded by 4 oxygens at 1.77(2) Å, 2 Ca at 3.06(2) Å and 4 Ga, Ge and Ca at 3.44(2), 3.74(2) and 3.78(5) Å, respectively. In the case of the Ge-modified 8 at% Yb:CNGG crystal, its EXAFS signal is similar to that of the CGGG reference and good agreement between the data and fit is obtained considering Ge^{4+} ions in the tetrahedral $24d$ sites of the CNGG garnet structure. Table S5 lists the bond distances obtained for the CGGG and Ge-modified 8 at% Yb:CNGG crystals.
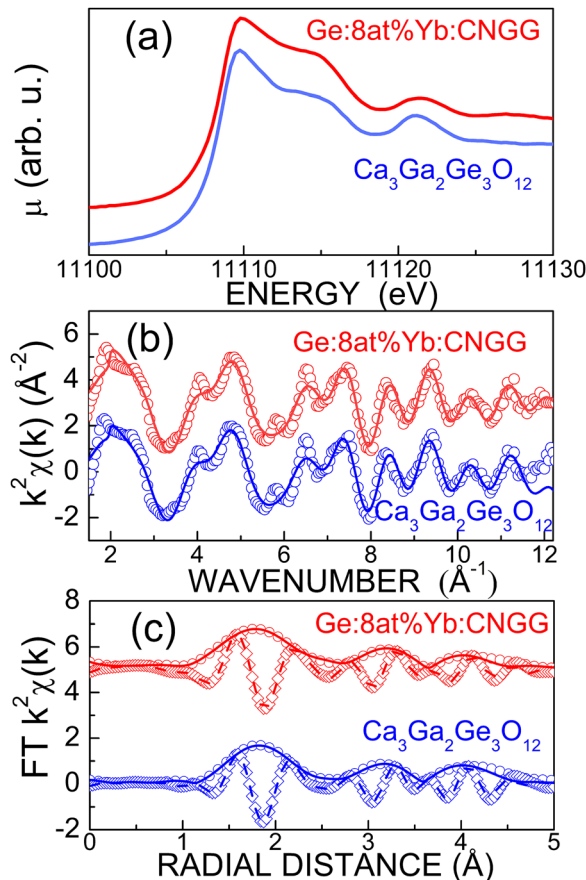

Fig. 5 Analysis of the X-ray absorption of the 20 at% Ge-modified 8 at% Yb:CNGG (red symbols and lines) and $Ca_3Ga_2Ge_3O_{12}$ (blue symbols and lines) crystals. (a) Normalised Ge K-edge XANES spectra (μ). (b) $k^2 \cdot \chi(k)$ weighted EXAFS spectra. (c) Real (circles and continuous lines) and imaginary (diamonds and dashed line) parts of the Fourier Transform (FT) of the $k^2\chi(k)$ signal in the phase-shifted scale. In (b) and (c), symbols are the experimental data and lines are the simulated fits. Plots are vertically shifted for clarity.

3.5.1.b. scXRD of Ge-modified Yb:CNGG. The Ge^{4+} site position in the CNGG garnet cannot be discerned exclusively from the scXRD data analysis because of the close atomic numbers of Ga (Z = 31) and Ge (Z = 32). However, once the Ge^{4+} position has been determined based on the XAS analysis as the $24d$ garnet site, and taking into account the cationic composition results from EPMA, the scXRD structure refinement of the Ge-modified 8 at% Yb:CNGG crystal was carried out. In the final refinement cycles, the procedure considered a fixed Nb^{5+} $24d$ occupancy (with a value similar to that obtained for previous CNGG crystals), whereas the Ga^{3+} and Ge^{4+} occupancies over the $24d$ sites were allowed to vary. The obtained $24d$ Ge^{4+} occupancy was in accordance with the EPMA analysis, as shown in Table 3 and Table S9. Later, by fixing these Ga^{3+} and Ge^{4+} occupancies, the Nb^{5+} population in the $24d$ site was refined. The last refinement cycle yielded the lowest discrepancy factor R_1 [$I > 2\sigma(I)$] = 0.0104. According to this, the number of $24d$ vacant sites was estimated as $\approx 3\%$. Table 2 and Table S8 include these data as well as the unit cell parameter, the oxygen positional coordinates, and Ca^{2+},

Yb^{3+}, Nb^{5+} and Ga^{3+} populations over the other available dodecahedral 24c and octahedral 16a garnet sites. Positive values of the anisotropic thermal displacements were obtained for all atoms.

3.5.1.c. OA of Yb^{3+} in Ge modified 8 at% Yb:CNGG. Fig. 3c shows the OA of the Ge-modified 8 at% Yb:CNGG crystal measured at $T = 6$ K. Firstly, it is worth noting the strong decrease in intensity of the $\lambda = 973$ nm band formerly associated with the presence of a 24d vacancy nearby Yb^{3+}. The main band at $\lambda = 971.1$ nm appears broader than in the unmodified 8 at% Yb:CNGG crystal because of the evident presence of a band shoulder at the high-energy band wing. The band spectral decomposition evidences a band contribution at $\lambda = 969.6$ nm (10314 cm^{-1}), with the details presented in SI Fig. S14 and Table S10. It is important to note that this new band induced by the presence of Ge^{4+} appears at a higher energy than that induced by any other studied cations with lower oxidation states in the Yb^{3+} neighbourhood.

3.5.2. Ti^{4+}-modified 8 at% Yb:CNGG. The Ti^{4+} site in CNGG garnets is uncertain. In some natural and synthetic Si garnets, Ti is found simultaneously in the octahedral and tetrahedral sites,[51–53] and thus a specific study of the CNGG case is required. The incorporation of Ti^{4+} into the CNGG lattice was first assessed in powders prepared by SSS (24 h annealing at 1000 °C, followed by a 24 h annealing period at 1150 °C). The Ti atomic percentage is expressed with regard to the total Nb amount. XRD of these powders shows that with up to 10 at% of Ti composition, only the garnet phase is formed. In the case of larger Ti concentrations, although the garnet phase is dominant, a second phase is observed; see SI Fig. S5a. Thus, the Ti composition in the single crystal was limited to 10 at% with respect to Nb, and two crystals were grown with the following compositions: 5 at% Ti-modified 8 at% Yb:CNGG, $Ca_{2.76}Yb_{0.24}Nb_{1.6031}Ti_{0.0844}Ga_{3.1875}O_{12}$, and 10 at% Ti-modified 8 at% Yb:CNGG, $Ca_{2.76}Yb_{0.24}Nb_{1.5185}Ti_{0.169}Ga_{3.1875}O_{12}$. The results obtained are similar for both Ti compositions, and thus here we present only those related to the latter composition. The presence of Ti^{3+} either in the as-grown or even in vacuum-annealed CNGG crystals is ruled out because the characteristic photoluminescence associated with its d^1 electronic configuration was not observed.

3.5.2.a. XAS of Ti^{4+} in 8 at% Yb:CNGG. The XANES spectrum of 10 at% Ti-modified 8 at% Yb:CNGG was collected, along with that of other reference oxides with 6-fold ($SrTiO_3$) or 4-fold (Y_2TiMoO_8 and α'-Ba_2TiO_4) Ti–O coordinations. $SrTiO_3$ powder was obtained by grinding a bulk single crystal, while α'-Ba_2TiO_4 and Y_2TiMoO_8 microcrystals were synthesised following previously described methods,[54,55] and SI Sections SI4.2 and S4.3 present the details.

Fig. 6a depicts a comparison of the collected XANES. Previous XAS studies have established that the XANES spectra of 4-fold coordinated Ti is characterized by a well-resolved peak at 4969.8 ± 1.0 eV, which is absent in the XANES spectrum of 6-fold coordinated Ti.[56] This XANES peak is clearly observed in Fig. 6a for α'-Ba_2TiO_4 and Y_2TiMoO_8, but it is not observed in the 10 at% Ti-modified 8 at% Yb:CNGG crystal; thus, we can confidently conclude that Ti^{4+} does not occupy the 24d
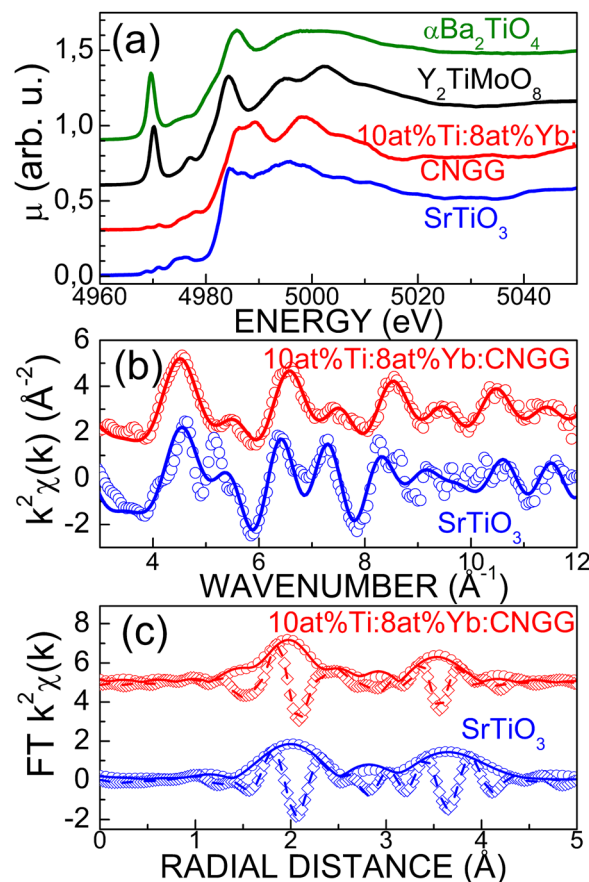
Fig. 6 Ti K-edge XAS results for 10 at% Ti-modified 8 at% Yb:CNGG (red) and reference compounds: tetrahedral Ti in α'-Ba_2TiO_4 (green) or Y_2TiMoO_8 (black) and the octahedral Ti in $SrTiO_3$ (blue) crystals. (a) Normalised XANES spectra (μ). (b) $k^2\cdot\chi(k)$ weighted EXAFS oscillations. (c) Real (circles and continuous lines) and imaginary (diamonds and dashed lines) parts of the Fourier transform (FT) of the $k^2\chi(k)$ signals in the phase-shifted scale. In (b) and (c), the data are the symbols and the fits the lines. Plots are vertically shifted for clarity.

tetrahedral site of the garnet. Given that dodecahedral Ti occupation is not known in garnets, the only remaining possibility for Ti in CNGG is the octahedral 16a site.

Fig. 6b shows the EXAFS spectra of the 10 at% Ti-modified 8 at% Yb:CNGG crystal in comparison to that of the octahedral Ti (CN = 6) in the $SrTiO_3$ perovskite. The fit of the EXAFS spectra at the Ti K-edge of the $SrTiO_3$ reference agrees with the known values for the perovskite with Ti^{4+} ions surrounded by 6 oxygens at 1.96(2) Å, 8 Sr cations at 3.40(3) Å and 6 Ti cations at 4.00(6) Å. In the case of Ti in the CNGG single crystal, a good fit of the experimental EXAFS data is obtained considering Ti^{4+} surrounded by 6 oxygens at a distance of 1.96(2) Å, followed by 6 Ca cations at 3.41(4) Å and 6 Ga cations at 3.44(3) Å. These radial distances are evidenced in the EXAFS weighted FT, as shown in Fig. 6c. The comparison of the EXAFS-derived Ti radial bond distances with that expected in the three crystallographic sites of the garnet, as seen in SI Table S2, agrees exclusively for Ti^{4+} cations occupying the octahedral 16a site of the CNGG garnet lattice.

3.5.2.b. scXRD of Ti-modified 8 at% Yb:CNGG. In the case of CNGG, the radius mismatch for the replacement of Nb^{5+}/Ga^{3+} with Ti^{4+} is $\Delta r = -5.47\%$ and $\Delta r = -10.64\%$ for the 16*a* and 24*d* sites, respectively; see in SI Table S1. The comparison of the lattice parameters of 10 at% Ti-modified 8 at% Yb:CNGG, *a* = 12.4720(3) Å, and that of 8 at% Yb:CNGG, *a* = 12.4728 Å, as shown in SI Table S2, shows that basically there is no change, which suggests the incorporation of Ti in the site with the smallest radius mismatch, *i.e.* the octahedral 16*a* site, in accordance with previous XAS results.

The refinement of the scXRD results given in Table 2 provides an occupancy factor of 0.092 of Ti in the 16*a* site, *i.e.*, titanium is incorporated during crystal growth with a segregation coefficient close to unity. Both the dodecahedral and octahedral sites are totally occupied, but still 6% of the tetrahedral sites are vacant. Although the Ca and Yb populations on the 24*c* site are not affected by the incorporation of Ti, as shown in Table 3, the relative Nb/Ga distribution over the 16*a* site favours the incorporation of Nb^{5+}. On the contrary, in the 24*d* site, in which Ti is absent, Nb^{5+} is basically displaced by Ga^{3+}, while the population of tetrahedral vacancies (6%) remains close to that found in 8 at% Yb:CNGG, *i.e.* 7.5%, as shown in Table 3.

3.5.2.c. OA of Ti-modified 8 at% Yb:CNGG. Fig. 3d shows a comparison of the $0 \rightarrow 0'$ OA of Yb^{3+} measured at $T = 6$ K in 10 at% Ti-modified 8 at% Yb:CNGG and in 8 at% Yb:CNGG single crystals. For ease of comparison, both spectra have been normalised to a unit area. It is evident that both spectra are equal, and in particular the optical absorption band at $\lambda = 973$ nm is observed in both cases with rather similar intensity as expected due to the slight change in the 24*d* vacancy density determined based on the scXRD and PALS (Table 1) results. New Yb^{3+} OA bands are not observed but the increase in the intensity of the $\lambda = 971.1$ nm band is consistent with the enhancement in the Ga^{3+} OF in the 24*d* site. One can conclude that the modification of the cationic charge over the 16*a* garnet site (Ga^{3+}/Nb^{5+} substitution by Ti^{4+}) has no, or very little, influence on the CF on Yb^{3+}.

3.6. Q = 5+: Nb⁵⁺ in Yb:CNGG

Nb^{5+} is a constituent element of the CNGG crystals, which in undoped CNGG is distributed in the 16*a* and 24*d* sites in the ratio of 0.86/0.14. Yb^{3+} doping with high concentrations (>5 at%) displaces this ratio basically to confine all Nb^{5+} in the 16*a* octahedral site, and in parallel the concentration of 24*c* dodecahedral vacancies decreases near zero, while that of the 24*d* tetrahedral ones remains constant in the OF ≈ 0.075 level, as shown in Table 3.

The 6 K OA spectrum of Yb^{3+} changes very little with an increase in Yb concentration, suggesting that the minor amount of Nb^{5+} in the tetrahedral 24*d* site has a minimal contribution to the Yb^{3+} band shape. Basically, no tetrahedral Nb^{5+} is found in the 8 at% Yb-doped CNGG crystals, and both the amount of tetrahedral vacancies and the intensity of the $\lambda = 973$ nm OA band remain independent of the Yb concentration.

Attempts to dope the CNGG crystals with V^{5+} as an alternative pentavalent cation failed due to the lack of incorporation

of this ion into the garnet lattice, as shown in SI Fig. S7f, and correspondingly no difference in the cryogenic ($T = 6$ K) OA of Yb^{3+} was found between the nominally V-modified and non-modified 8 at% Yb:CNGG crystals, as shown in SI Fig. S17.

3.7. Room temperature fluorescence

Fig. 7 shows the Yb^{3+} luminescence of the Li-, 30 at% Mg- and 10 at% Ge-modified 8 at% Yb:CNGG single crystals. The purpose of this characterization is to determine if the decrease in the tetrahedral cationic vacancies has any effect on the observed bandwidth. For this purpose, plate samples with the same thickness (≈ 0.2 mm) were tested under identical experimental conditions, *i.e.* keeping the same excitation power level (130 mW) and wavelength conditions ($\lambda_{EXC} = 971.6$ nm), as well as monochromator slits (0.2 mm).

Fig. 7a and 7b show that the Li- and 30 at% Mg-modified 8 at% Yb:CNGG single crystals have slightly narrower Yb emission than the unmodified 8 at% Yb:CNGG crystal, respectively. On the contrary, in the 10 at% Ge-modified 8 at% Yb:CNGG crystal, the intensity of the Yb^{3+} emission is observed to increase in the low-energy band side in comparison to the unmodified 8 at% Yb:CNGG crystal.

4. Discussion

The heterovalent substitutional strategy used in the present work pursues the replacement of the 5+ and 3+ electric charges
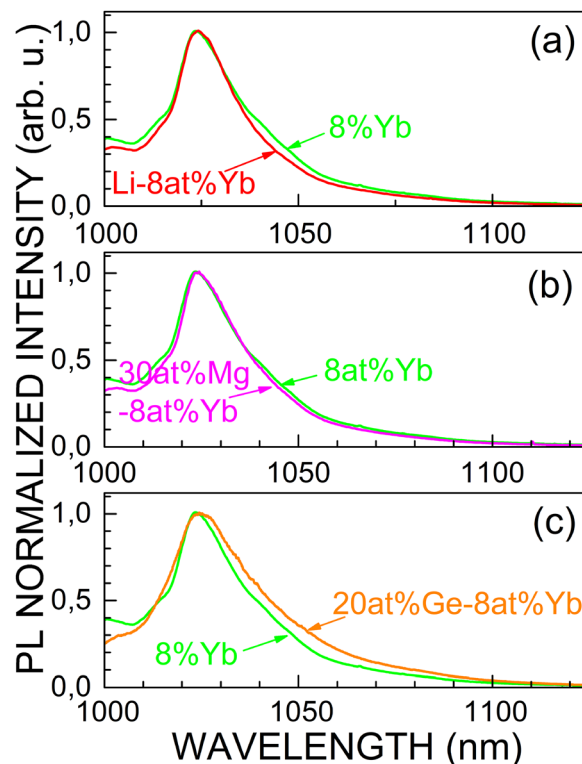

Fig. 7 Comparison of the room temperature fluorescence of the 8 at% Yb:CNGG single crystals modified with (a) Li, (b) 30 at% Mg, and (c) 20 at% Ge. All spectra have been excited at $\lambda = 971.6$ nm with a TiSa laser.

of the constituent Nb and Ga elements with other electric charges in the range of 1+ to 5+. For this purpose, the growth of CNGG single crystals modified with Li^+, Mg^{2+}, Si^{4+}, Ge^{4+}, Ti^{4+}, and V^{5+} cations was attempted. Only Li^+, Mg^{2+}, Ge^{4+}, and Ti^{4+} produced single crystals of the garnet phase. The other cations either do not incorporate into the crystal, as in the case of V^{5+}, or the polycrystalline precursor and solidified materials are not exclusively the garnet phase, as in the case of Si^{4+}. Nonetheless, the range of electric charges, namely, from 0 to 4+, that we are presenting for the successfully grown CNGG single crystals allows us to disclose their influence on the optical properties of Yb^{3+}.

Firstly, it must be noted that the CNGG composition is sensitive to the growth conditions as well as to the presence of lanthanide doping elements. In particular, the incorporation of Yb not only reduces the cell volume but also has a deep influence on the density of cationic vacancies and the incorporation of Nb into the tetrahedral 24d site.[10,11] Therefore, any comparison of the changes induced by the incorporation of other modifier cations in Yb-doped crystals must employ the proper Yb:CNGG composition as the reference rather than the undoped CNGG single crystal. To compare the different modified Yb:CNGG crystals, we selected a nominal (melt) 8 at% Yb composition in the dodecahedral 24c site for all the presented crystals. However, the segregation coefficient of Yb is also sensitive to other co-dopants and may change from 0.9 to 1.1,[13] which should be considered to explain minor fluctuations in the observed results.

Further, the Ga volatility from the melt during the Czochralski growth, which is also observed in other Ga-based crystals,[57,58] leads to a small depletion of the Ga/Nb ratio as the crystal is pulled out from the melt during the growth process, as shown in SI Fig. S12a. Given that the crystal becomes enriched in Nb^{5+} ions, an increase in cationic vacancy density can be expected to maintain charge neutrality, which could explain the increase in the relative intensity of the 6 K $0 \rightarrow 0'$ Yb^{3+} OA band at $\lambda = 973$ nm observed from the seed to the end of the crystal, as shown in SI Fig. S13.

From the point of view of cationic incorporation into the CNGG lattice, the simplest cases to be considered are Ge^{4+} and Ti^{4+}. The similarity of the XAS results of Ge-modified 8 at% Yb:CNGG and the reference $Ca_3Ga_2Ge_3O_{12}$ crystal, as shown in Fig. 5, indicates unequivocally that Ge in CNGG sits exclusively in the 24d tetrahedral garnet site (as in the reference). Alternatively, the absence of a peak at 4969.8 eV in the XANES spectrum of the Ti-modified 8 at% Yb:CNGG crystal, as shown in Fig. 6a, rules out its presence in the tetrahedral garnet site, and the similarity of the XANES and EXAFS spectra for the Ti-modified 8 at% Yb:CNGG and $SrTiO_3$ clearly indicates that Ti^{4+} sits exclusively in the octahedral 16a garnet site. Thus, Ge^{4+} and Ti^{4+} are each in a different site of the garnet lattice, and their influence on the Yb^{3+} $0 \rightarrow 0'$ OA observed at $T = 6$ K is quite different. Although Ge^{4+} induces a reduction in the intensity of the $\lambda = 973$ nm OA band and creates a new one at $\lambda = 969.9$ nm, as shown in Fig. 3c, the presence of Ti^{4+} does not introduce a significant change in the energy position of the Yb^{3+} $0 \rightarrow 0'$ OA, as shown in Fig. 3d. Therefore, it can be concluded that the most important contribution to the CF on Yb^{3+} comes from the occupancy of the 24d tetrahedral sites at the shortest distances to Yb^{3+} in the 24c sites, as shown in SI Fig. S1 and Table S3. In fact, there are two edge-sharing 24d tetrahedra linked to the 24c dodecahedral polyhedron at the shortest intercationic distance of 3.1242 Å, which are expected to create the strongest CF interaction with Yb^{3+}.

Li is another cation in CNGG that sits exclusively in the tetrahedral 24d garnet site.[11] The CLNGG single crystals were grown from a melt composition much closer to the stoichiometric garnet formula than CNGG, i.e. the amount of nominal cationic vacancies in the precursor CLNGG composition is five-times smaller ($x = 0.025$) than in the CNGG precursor ($x = 0.125$). The reduction in the cationic vacancy density in CLNGG with regard to CNGG was previously determined by scXRD refinements,[11] and now it is experimentally demonstrated by the PALS results presented in Section 3.1.1. Table 1 shows that the intensity of the long-lived lifetime for positron annihilation in the cationic vacancies is reduced by $\approx 16.6\%$ from CNGG to CLNGG, and by 6.2% from 8 at% Yb:CNGG to 8 at% Yb:CLNGG. On the contrary, in the case of Ti-modified 8 at% Yb:CNGG, the difference with regard to the unmodified 8 at% Yb:CNGG is less than 1%. Clearly, the incorporation of Li reduces the vacancy density upon the site it enters, i.e. the tetrahedral 24d garnet site. In parallel to this cationic vacancy reduction, Fig. 3a shows a decrease in the intensity of the $\lambda = 973$ nm Yb^{3+} OA band observed at $T = 6$ K upon the incorporation of Li^+. Thus, in parallel to the previous discussion for Ge^{4+}, this decrease in the Yb^{3+} OA must be ascribed to the reduction in vacant tetrahedral sites in the first neighbor cationic shell around the dodecahedral Yb^{3+}. Further, the OA intensity loss at $\lambda = 973$ nm is parallel to the appearance of a new band at 971.9 nm in 8 at% Yb:CLNGG.

A decrease in the $\lambda = 973$ nm band intensity and the appearance of a new Yb^{3+} OA band at $\lambda = 971.3$ nm are also observed for the 30 at% Mg-modified 8 at% Yb:CNGG single crystal. In this case, the reduction in the $\lambda = 973$ nm band intensity is clear but its amount is smaller than that for the Li^+ or Ge^{4+} cases. Unlike the incorporation of Li^+, Ti^{4+} or Ge^{4+}, the Mg^{2+} in 8 at% Yb:CNGG crystal is not located at a single site. The Mg-modified Yb:CNGG XANES spectrum in Fig. 4a shows features corresponding to the three garnet sites, and the scXRD refinement quantified this distribution as 17% (24c), 8% (16a) and 75% (24d) of the total Mg composition. The PALS results elucidate that the vacancy density in the Mg-modified 8 at% Yb:CNGG is intermediate between that of 8 at% Yb:CNGG and 8 at% Yb:CLNGG; thus, one would expect a lower reduction in the $\lambda = 973$ nm OA band intensity than in the Li and Ge cases. In fact, this is observed in the comparison of Fig. 3a and c with 3b. Thus, the presence of Mg^{2+} in the 24d tetrahedral site induces similar spectroscopic changes in the Yb $0 \rightarrow 0'$ OA than that observed for other heterovalent cations in this same site, while the Mg fraction in the dodecahedral and octahedral sites would behave as the Ti^{4+} case, i.e. they do not have much influence on the Yb^{3+} energy level position.

Ga^{3+} is the most abundant cation on the 24d tetrahedral site (OF ≈ 0.8). It even displaces 24d Nb^{5+} to compensate for the

increase in electric charge associated with Yb^{3+} doping in the Ca^{2+} site, reaching OF > 0.9. The most intense Yb $0 \to 0'$ band at $\lambda = 971.1$ nm must be associated with the most abundant environment around Yb, *i.e.*, where all the tetrahedral and octahedral first neighbors are occupied by $24d$ Ga^{3+} and $16a$ Nb^{5+}, respectively.

In summary, we have shown that the different Yb^{3+} $0 \to 0'$ OA bands observed at $\lambda = 973$ nm, 971.9 nm, 971.3 nm, 971.1 nm and 969.6 nm can be correlated with the presence of a vacancy ($Q = 0$), Li^+ ($Q = 1$), Mg^{2+} ($Q = 2$), Ga^{3+} ($Q = 3$) and Ge^{4+} ($Q = 4$) in the tetrahedral garnet site, respectively, while the presence of Ti^{4+} in the octahedral site substituting Nb^{5+} has no observable effect on the energy position of Yb^{3+} OA. This shows that the main contribution to the CF on the Yb^{3+} sites arises from the electric charges at the closest tetrahedra.

Nb^{5+} is indeed found in the tetrahedral sites of CNCG. According to the findings described above, it could be expected that it would contribute with a Yb^{3+} $0 \to 0'$ OA band at $\lambda <$ 969.6 nm. However, the Nb $24d$ OF is only 10%, and as already mentioned, the presence of Yb^{3+} decreases the Nb $24d$ OF to 0.5–0.3%. It seems likely that such a minor amount of Nb^{5+} in the tetrahedral site cannot be resolved in the experimental spectra despite the high spectral resolution used.

From a mode-locked lasing point of view, the interest is to find how the changes introduced in the energy of the Yb^{3+} electronic levels may modify the fluorescence bandwidth. Fig. 7a and b show that in parallel with the disappearance of the $\lambda = 973$ nm $0 \to 0'$ OA band, the Yb^{3+} fluorescence becomes slightly narrower. This is consistent with the reduction in the range of energies exhibited by the available Yb centres in each case including 1.2744–1.2769 eV ($\lambda = 973$–971.1 nm) for Yb:CNGG *versus* 1.2758–1.2769 eV ($\lambda = 971.9$–971.1 nm) in the Yb:CLNGG case. Thus, elimination of the tetrahedral vacancies present in CNGG would not be desirable for a reduction in the laser pulse duration. However, Fig. 7c shows that in the 20 at% Ge-modified 8 at% Yb:CNGG case, some band broadening is observed despite the fact that Ge in the tetrahedral $24d$ garnet site also reduces the concentration of cationic vacancies of this site. Somehow, the new OA observed at $\lambda = 969.9$ nm associated with the presence of a 4+ charge in the $24d$ site is able to compensate for the loss of centres with absorption at $\lambda = 973$ nm. Nevertheless, this preliminary conclusion must be taken with caution because the actual Yb concentration in the crystals is reduced from 9.1 at% in nominally 8 at% Yb:CNGG to 7–7.5 at% in the Li- or Mg-modified 8 at% Yb:CNGG crystals; on the contrary, in the case of the used Ge-modified crystal, the Yb concentration increases up to 12.8 at%. These modifications in the Yb concentration may have an influence in the Yb^{3+} fluorescence profile due to the emission reabsorption. Future work is required to confirm the Yb^{3+} fluorescence profiles free of fluorescence reabsorption as well as to extend these concepts to the most common 3–5 at% Yb concentration level used in laser applications.

Several works, some of them described in the Introduction, have studied isovalent substitutions in YAG single crystals or transparent ceramics[59] to modify the Yb^{3+} electronic level energies but without great success. Heterovalent substitutions in YAG have been rarely attempted. One such case was the mixing of Yb:YAG with $Mn_3Al_2(SiO_4)_3$ garnets.[60] In the latter work, the heterovalent substitutions of Y^{3+} by Mn^{2+} and Al^{3+} by Si^{4+} were attempted. Unfortunately, the incorporation of Si into the crystal was not detected, as in the current case of Si-modified CNGG, as shown in SI Sections S2.2 and S8.2; thus, no modification of the tetrahedral garnet site was achieved. Conversely, Mn^{2+} sits in the dodecahedral site, or it could also be distributed in the octahedral site; see in SI Fig. S1. However, as discussed above, the electric charge modification on these sites has little influence on the Yb^{3+} $0 \to 0'$ OA. As a result, the Yb^{3+} fluorescence bandwidth obtained through this YAG modification was only FWHM = 140 cm^{-1}, which is somehow higher than in Yb:YAG (FWHM = 85 cm^{-1}), but far below that observed in Yb:CNGG (FWHM = 220 cm^{-1}). From this perspective, the heterovalent substitution of Al^{3+} with Ge^{4+}, rather than Si^{4+}, would seem more favourable, although in the ceramic processing, other factors, such as refractive index matching, could limit the transparency.

5. Conclusions

Single crystal growth of 8 at% Yb-doped $Ca_3(NbGa\square)_5O_{12}$-type garnet (CNGG) modified with other optically silent cations was possible for Li^+, Mg^{2+}, Ge^{4+} and Ti^{4+} within some incorporation limits of $\approx 10\%$ of the corresponding site occupancy. These heterovalent substitutions of the trivalent (Ga^{3+}) and pentavalent (Nb^{5+}) constituent cations simultaneously introduce some lattice strain and electric charge misfit in the CNGG crystalline lattice. The $^2F_{7/2}(0) \to {}^2F_{5/2}(0')$ transition (shortly $0 \to 0'$) of Yb^{3+} measured at $T = 6$ K has been found to be a sensitive local probe for the crystal field (CF) changes introduced by these crystal modifications.

The combined X-ray absorption (XAS) and single crystal diffraction (scXRD) analyses of Mg-, Ge- and Ti-modified Yb:CNGG single crystals, along with previous studies on the Li case, show that Li and Ge are found exclusively in the tetrahedral $24d$ crystal garnet site and Ti is found exclusively in the octahedral $16a$ site, while Mg distributes in the three (dodecahedral, $24c$; octahedral, $16a$; and tetrahedral $24d$) garnet sites.

Previous scXRD studies showed that cationic vacancies in the three crystal sites are characteristic of undoped CNGG, but in CNGG crystals doped with Yb in excess of 5 at%, they are found with significance only in the tetrahedral $24d$ site. This view is now corroborated by positron annihilation lifetime spectroscopy (PALS), which shows a significant reduction in the intensity of the long-lived lifetime characteristic of positron annihilation at the vacancy defects upon Yb doping. The PALS results show a further reduction in the Yb:CNGG vacancy density when the crystal incorporates Li (as anticipated by scXRD in previous works), and to a lesser extent, Mg, but Ti incorporated in the octahedral $16a$ site does not reduce the concentration of cationic vacancies present in Yb:CNGG.

The $0 \to 0'$ Yb^{3+} optical absorption (OA) shows several bands related to the coexistence of several Yb^{3+} centres in the disordered

CNGG host. The most intense OA band of Yb:CNGG at $\lambda = 971.1$ nm should be related to the most common Yb environment associated with the exclusive presence of Ga^{3+} in the nearest-to-Yb $24d$ tetrahedral site. Another less intense but well-resolved OA band at $\lambda = 973$ nm is also found in the non-modified Yb:CNGG crystals. The intensity of the latter band increases as the crystal growth proceeds, i.e. its intensity is larger at the crystal end than at the beginning, which is associated with a decrease in Ga incorporation as the growth proceeds. This minor band at $\lambda = 973$ nm is ascribed to the presence of an empty tetrahedral vacancy with zero electric charge nearby Yb^{3+}.

Heterovalent cations incorporated in the tetrahedral site, such as Li^+, Mg^{2+} and Ge^{4+}, simultaneously reduce the cationic vacancy density on this site and the intensity of the $\lambda = 973$ nm Yb^{3+} OA. Conversely, the incorporation of Ti^{4+} in the octahedral site does not modify the OA Yb^{3+} spectra. The modification of the Yb^{3+} environment produces new OA bands at $\lambda = 971.9$ nm for Li^+, $\lambda = 971.3$ nm for Mg^{2+}, and $\lambda = 969.6$ nm for Ge^{4+}. Consequently, the position of the $0 \rightarrow 0'$ Yb^{3+} OA shifts to a higher energy (shorter wavelength) as the cationic electric charge in the Yb^{3+} neighbourhood increases. This shows that heterovalent substitution in the tetrahedral $24d$ site of the garnet structure is the main driving force to change the CF on Yb and could be implemented in laser garnets (YAG and others) either by crystal growth or ceramic processing with the potential of larger inhomogeneous fluorescence broadening than that in the previously widely conducted isovalent substitution strategy.

Author contributions

All authors contributed to conceptualization, investigation, data analysis and funding acquisition. The manuscript was written through contributions of all authors.

Conflicts of interest

There are no conflicts to declare.

Data availability

The data supporting this study have been included within the article and the corresponding supplementary information (SI) and CIF materials. Further data are available from the corresponding author upon reasonable request.

Supplementary information about garnet crystallography, growth of modified-Yb:CNGG and XAS reference single crystals, EXAFS and XRD analyses, as well as further optical spectroscopic characterizations, is available. See DOI: https://doi.org/10.1039/d5tc03824c.

CCDC 2448685, 2448696 and 2448697 contain the supplementary crystallographic data for this paper.[61a-c]

Acknowledgements

References

1 U. Keller, *Ultrafast Lasers. A comprehensive introduction to fundamental principles with practical applications*, Springer, Switzerland AG, 2021, ch. 2., DOI: 10.1007/978-3-030-82532-4, ISBN 978-3-030-82531-7.

2 C. Hönninger, R. Paschotta, M. Graf, F. Morier-Genoud, G. Zhang, M. Moser, S. Biswal, J. Nees, A. Braun, G. A. Mourou, I. Johannsen, A. Giesen, W. Seeber and U. Keller, Ultrafast ytterbium-doped bulk lasers and laser amplifiers, *Appl. Phys. B*, 1999, **69**, 3–17, DOI: 10.1007/s003400050762.

3 J. Drs, J. Fischer, N. Modsching, F. Labaye, V. J. Wittwer and T. Sudmeyer, Sub-30-fs Yb:YAG thin-disk laser oscillator operating in the strongly self-phase modulation broadened regime, *Opt. Express*, 2021, **29**, 35929, DOI: 10.1364/OE.440196.

4 J. Dong, K. Ueda and A. A. Kaminskii, Continuous-wave and Q-switched microchip laser performance of $Yb:Y_3Sc_2Al_3O_{12}$ crystals, *Opt. Express*, 2008, **16**(8), 5241–5251, DOI: 10.1364/OE.16.005241.

5 J. Koerner, C. Vorholt, H. Liebetrau, M. Kahle, D. Kloepfel, R. Seifert, J. Hein and M. C. Kaluza, Measurement of temperature-dependent absorption and emission spectra of Yb:YAG, Yb:LuAG, and $Yb:CaF_2$ between 20 °C and 200 °C and predictions on their influence on laser performance, *J. Opt. Soc. Am. B*, 2012, **29**(9), 2493–2502, DOI: 10.1364/JOSAB.29.002493.

6 H. Yu, K. Wu, B. Yao, H. Zhang, Z. Wang, J. Wang, Y. Zhang, Z. Wei, Z. Zhang, X. Zhong and M. Jiang, Growth and characteristics of Yb-doped $Y_3Ga_5O_{12}$ laser crystal, *IEEE J. Quantum. Electron.*, 2010, **46**(12), 1689–1695, DOI: 10.1109/JQE.2010.2059373.

7 M. O. Ramírez, L. E. Bausá, E. Cavallia and E. Bovero, Optical spectroscopy of Yb^{3+}-doped $Ca_3Sc_2Ge_3O_{12}$ garnet crystal, *J. Appl. Phys.*, 2006, **99**, 013507, DOI: 10.1063/1.2150261.

8 J. O. Álvarez-Pérez, J. M. Cano-Torres, A. Ruiz, M. D. Serrano, C. Cascales and C. Zaldo, Correction: A roadmap for laser optimization of $Yb:Ca_3(NbGa)_5O_{12}$-CNGG-type single crystal garnets, *J. Mater. Chem. C*, 2021, **9**, 6945–6946, DOI: 10.1039/d1tc90105b.

9 V. Lupei, A. Lupei, C. Gheorghe, L. Gheorghe, A. Achim and A. Ikesue, Crystal field disorder effects in the optical spectra of Nd^{3+} and Yb^{3+}-doped calcium lithium niobium gallium garnets laser crystals and ceramics, *J. Appl. Phys.*, 2012, **112**, 063110, DOI: 10.1063/1.4752070.

10 E. Castellano-Hernández, M. D. Serrano, R. J. Jiménez-Riobóo, C. Cascales, C. Zaldo, A. Jezowski and P. A. Loiko, Na modification of lanthanide doped $Ca_3Nb_{1.5}Ga_{3.5}O_{12}$-type laser garnets: Czochralski crystal growth and characterization, *Cryst. Growth Des.*, 2016, **16**, 1480–1491, DOI: 10.1021/acs.cgd.5b01607.

11 M. D. Serrano, J. O. Álvarez-Pérez, C. Zaldo, J. Sanz, I. Sobrados, J. A. Alonso, C. Cascales, M. T. Fernández-Díaz and A. Jezowski, Design of Yb^{3+} optical bandwidths by crystallographic modification of disordered calcium niobium gallium laser garnets, *J. Mater. Chem. C*, 2017, **5**, 11481, DOI: 10.1039/C7TC02760E.

12 C. Gheorghe, S. Hau, L. Gheorghe, F. Voicu, M. Greculeasa, A. Broasca and G. Stanciu, RE^{3+}-doped $Ca_3(Nb,Ga)_5O_{12}$ and $Ca_3(Li,Nb,Ga)_5O_{12}$ crystals (RE = Sm, Dy, and Pr): A review of current achievements, *Materials*, 2023, **16**, 269, DOI: 10.3390/ma16010269.

13 J. O. Álvarez-Pérez, J. M. Cano-Torres, A. Ruiz, M. D. Serrano, C. Cascales and C. Zaldo, A roadmap for laser optimization of $Yb:Ca_3(NbGa)_5O_{12}$-CNGG-type single crystal garnet, *J. Mater. Chem. C*, 2021, **9**, 4628–4642, DOI: 10.1039/D0TC05718E.

14 J. I. Goldstein, D. E. Newbury, P. Echlin, D. C. Joy, A. Roming, C. Lyman, C. Fiori and E. Lifshin, *Scanning Electron Microscopy and X-ray Microanalysis*, Plenum, New York, 1992.

15 M. Yamawaki, Y. Kobayashi, K. Hattori and Y. Watanabe, Novel system for potential nondestructive material inspection using positron annihilation lifetime spectroscopy, *Jpn. J. Appl. Phys.*, 2011, **50**, 086301, DOI: 10.1143/JJAP.50.086301.

16 J. Kansy and D. Giebel, Study of defect structure with new software for numerical analysis of PAL spectra, *J. Phys: Conf. Ser.*, 2011, **265**, 012030, DOI: 10.1088/1742-6596/265/1/012030.

17 R. Kraus-Rehberg and H. S. Leipner, *Positron Annihilation in Semiconductor: Defect Studies*, Springer-Verlag, Berlin/Heidelberg, 1st edn, 2010, p. 13.

18 M. Kitaura, Y. Taira and S. Watanabe, Characterization of imperfections in scintillator crystals using gamma-ray induced positron annihilation lifetime spectroscopy, *Opt. Mater: X*, 2022, **14**, 100156, DOI: 10.1016/j.omx.2022.100156.

19 D. Vantelon, N. Trcera, D. Roy, T. Moreno, D. Mailly, S. Guilet, E. Metchalkov, F. Delmotte, B. Lassalle, P. Lagarde and A. M. Flank, The LUCIA beamline at SOLEIL, *J. Synchrotron Radiat.*, 2016, **23**, 635–640, DOI: 10.1107/S1600577516000746.

20 L. Simonelli, C. Marini, W. Olszewski, M. Ávila Pérez, N. Ramanan, G. Guilera, V. Cuartero and K. Klementiev, CLAESS: The hard X-ray absorption beamline of the ALBA CELLS Synchrotron, *Cogent Phys.*, 2016, **3**(1), 1–10, DOI: 10.1080/23311940.2016.1231987.

21 B. Ravel and M. Newville, ATHENA, ARTEMIS, HEPHAESTUS: Data Analysis for X-Ray Absorption Spectroscopy Using IFEFFIT, *J. Synchrotron Radiat.*, 2005, **12**(4), 537–541, DOI: 10.1107/S0909049505012719.

22 SHELXTL (V 6.10) Software Package, Siemens Energy and Automation Inc. Analytical Instrumentation.

23 K. Shimamura, M. Timoshechkin, T. Sasaki, K. Hoshikawa and T. Fukuda, Growth and characterization of calcium niobium gallium garnet (CNGG) single-crystals for laser applications, *J. Cryst. Growth*, 1993, **128**(1–4), 1021–1024, DOI: 10.1016/S0022-0248(07)80090-X.

24 Yu. K. Voronko, A. A. Sobol, A. Ya Karasik, N. A. Eskov, P. A. Rabochkina and S. N. Ushakov, Calcium niobium gallium and calcium lithium niobium gallium garnets doped with rare earth ions-effective laser media, *Opt. Mater.*, 2002, **20**, 197–209, DOI: 10.1016/S0925-3467(02)00063-0.

25 A. A. Kaminskii, E. L. Belokoneva, A. V. Butashin, K. Kurbanov, A. A. Markosyan, B. V. Mill, O. K. Nikol'skaya and S. É. Sarkisov, Crystal structure and spectral luminescence properties of the cation-deficient garnet $Ca_3(Nb,Ga)_2Ga_3O_{12}$-Nd, *Inorg. Mater.*, 1986, **22**(7), 927–936.

26 Y. Ono, K. Shimamura, Y. Morii, T. Fukuda and T. Kajinati, Structure analysis of a Ca–Nb–Ga garnet, *Phys. B*, 1995, **213**, 420–422, DOI: 10.1016/0921-4526(95)00176-A.

27 F. A. Selim, C. R. Varney, M. C. Tarun, M. C. Rowe, G. S. Collins and M. D. McCluskey, Positron lifetime measurements of hydrogen passivation of cation vacancies in yttrium aluminum oxide garnets, *Phys. Rev. B: Condens. Matter Mater. Phys.*, 2013, **88**, 174102, DOI: 10.1103/PhysRevB.88.174102.

28 K. Fujimori, M. Kitaura, Y. Taira, M. Fujimoto, H. Zen, S. Watanabe, K. Kamada, Y. Okano, M. Katoh, M. Hosaka, J. Yamazaki, T. Hirade, Y. Kobayashi and A. Ohnishi, Visualizing cation vacancies in $Ce:Gd_3Al_2Ga_3O_{12}$ scintillators by gamma-ray-induced positron annihilation lifetime spectroscopy, *Appl. Phys. Express*, 2020, **13**, 085505, DOI: 10.35848/1882-0786/aba0dd.

29 J. Dong and K. Lu, Noncubic symmetry in garnet structures studied using extended X-ray-absorption fine-structure spectra, *Phys. Rev. B: Condens. Matter Mater. Phys.*, 1991, **43**, 8808, DOI: 10.1103/PhysRevB.43.8808.

30 J. O. Álvarez-Pérez, J. M. Cano-Torres, M. D. Serrano, C. Cascales and C. Zaldo, A probe of the radiation field magnetic component based on octahedral Yb^{3+} in the CaNbGa garnet -CNGG- single crystal, *J. Mater. Chem. C*, 2020, **8**, 7882–7889, DOI: 10.1039/d0tc01608j.

31 R. Pappalardo and D. L. Wood, Spectrum of Yb^{3+} in yttrium gallium garnet, *J. Chem. Phys.*, 1960, **33**, 1734–1742, DOI: 10.1063/1.1731494.

32 S. Geller, Crystal chemistry of the garnets, *Z. Kristallogr.*, 1967, **125**, 1–47, DOI: 10.1524/zkri.1967.125.16.1.

33 J. Song, K. Song, J. Wei, H. Lin, J. Wu, J. Xu, W. Su and Z. Cheng, Ionic occupation, structures, and microwave dielectric properties of $Y_3MgAl_3SiO_{12}$ garnet-type ceramics, *J. Am. Ceram. Soc.*, 2017, **101**, 244–251, DOI: 10.1111/jace.15174.

34 N. Trcera, D. Cabaret, S. Rossano, F. Farges, A. Flank and P. Lagarde, Experimental and theoretical study of the structural environment of magnesium in minerals and silicate glasses using X-ray absorption near-edge structure, *Phys. Chem. Miner.*, 2009, **36**, 241–257, DOI: 10.1007/s00269-008-0273-z.

35 P. Ildefonse P, G. Calas, A. M. Flank and P. Lagarde, Low Z elements (Mg, Al, and Si) K-edge X-ray absorption spectroscopy in minerals and disordered systems, *Nucl. Instrum. Methods Phys. Res., Sect. B*, 1995, **97**, 172–175, DOI: 10.1016/0168-583X(94)00710-1.

36 D. Li, M. Peng and T. Murata, Coordination and local structure of magnesium in silicate minerals and glasses: Mg K-edge XANES study, *Can. Mineral.*, 1999, **37**, 199–206.

37 G. Sankar, D. Gleeson, C. R. A. Catlow, J. M. Thomas and A. D. Smith, The architecture of Mg(II) centres in MAPO-36 solid acid catalysts, *J. Synchrotron Radiat.*, 2001, **8**, 625–627, DOI: 10.1107/S0909049501000139.

38 H. Yang, R. Hazen and R. Downs, *et al.*, Structural change associated with the incommensurate-normal phase transition in akermanite, $Ca_2MgSi_2O_7$, at high pressure, *Phys. Chem. Miner.*, 1997, **24**, 510–519, DOI: 10.1007/s002690050066.

39 H. Mohammadi, R. M. Da Silva, A. Zeidler, L. V. D. Gammond, F. Gehlhaar and M. Jr. de Oliveira, *et al.*, Structure of diopside, enstatite, and magnesium aluminosilicate glasses: a joint approach using neutron and X-ray diffraction and solid-state NMR, *J. Chem. Phys.*, 2022, **157**(21), 214503, DOI: 10.1063/5.0125879.

40 C. Téqui, R. A. Robie, B. S. Hemingway, D. R. Neuville and P. Richet, Melting and thermodynamic properties of pyrope $(Mg_3Al_2Si_3O_{12})$, *Geochim. Cosmochim. Acta*, 1991, **55**, 1005–1010, DOI: 10.1016/0016-7037(91)90158-2.

41 J. Zhang and C. Herzberg, Melting of pyrope, $Mg_3Al_2Si_4O_{12}$, at 7-16 GPa, *Am. Mineral.*, 1994, **79**, 497–503.

42 B. V. Mills, Crystallisation of germanium and silicate garnets from solutions in molten salts, *Sov. Phys. Crystallogr.*, 1975, **19**(5), 653–655.

43 A. Agnesi, S. DellAcqua, A. Guandalini, G. Reali, A. Toncelli, M. Tonelli and E. Cavalli, Laser action in cw diode-pumped Nd:$Ca_3Sc_2Ge_3O_{12}$ crystal, *Appl. Phys. B*, 2000, **71**, 153–156, DOI: 10.1007/s003400000277.

44 J. P. M. Damen, J. A. Pistorious and J. M. Robertson, Calcium gallium germanium garnet as a substrate for magnetic bubble application, *Mater. Res. Bull.*, 1977, **12**, 73–78, DOI: 10.1016/0025-5408(77)90090-3.

45 E. J. Sharp, J. E. Miller, D. J. Horowitz, A. Linz and V. Belruss, Optical spectra and laser action in Nd^{3+} doped $CaY_2Mg_2Ge_3O_{12}$, *J. Appl. Phys.*, 1974, **45**, 4974–4979, DOI: 10.1063/1.1663166.

46 A. A. Setlur, W. J. Heward, Y. Gao, A. M. Srivastava, R. G. Chandran and M. V. Shankar, Crystal chemistry and luminescence of Ce^{3+}-doped $Lu_2CaMg_2(Si,Ge)_3O_{12}$ and its use in LED based lighting, *Chem. Mater.*, 2006, **18**, 3314–3322, DOI: 10.1021/cm060898c.

47 H. Mei, L. Zhang, C. Li, Z. Rao and L. Shu, Compositional design stability, and microwave dielectric properties in $Ca_3MgBGe_3O_{12}$ (B = Zr, Sn) garnet ceramics with tetravalent cations on B-site, *Ceram. Int.*, 2022, **48**, 4658–4664, DOI: 10.1016/j.ceramint.2021.11.001.

48 J. Chen, H. Yan, A. Kuwabara, M. D. Smith, Y. Iwasa, H. Ogino, Y. Matsushita, Y. Tsujimoto, K. Yamaura and H. zur Loye, Flux crystal growth, crystal structure, and optical properties of new germanate garnet $Ce_2CaMg_2Ge_3O_{12}$, *Front. Chem.*, 2020, **8**, 91, DOI: 10.3389/fchem.2020.00091.

49 J. E. Miller, E. J. Sharp and D. J. Horowitz, Optical spectra and laser action of Neodymium in a crystal $Ba_{0.25}Mg_{2.75}Y_2Ge_3O_{12}$, *J. Appl. Phys.*, 1972, **43**, 462–465, DOI: 10.1063/1.1661140.

50 J. J. Kas, F. D. Vila and J. J. Rehr, *The FEFF Code*, Wiley Online Library, Chester, UK, 2020, pp. 1–6; ISBN 9781119433941.

51 M. R. Ackerson, N. D. Tailby and E. B. Watson, XAFS spectroscopic study of Ti coordination in garnet, *Am. Mineral.*, 2017, **102**, 173–183, DOI: 10.2138/am-2017-5633.

52 V. Cantavella, J. Carda, G. Monros, M. A. Tena, P. Escribano and J. Alarcon, Zr^{4+} and Ti^{4+} substitution in gallium garnets, *J. Mater. Chem.*, 1993, **3**(10), 1059–1064, DOI: 10.1039/JM9930301059.

53 H. Yamane and T. Kawano, Preparation, crystal structure and photoluminescence of garnet-type calcium tin titanium aluminates, *J. Solid State Chem.*, 2011, **184**, 965–970, DOI: 10.1016/j.jssc.2011.02.016.

54 J. A. Bland, The crystal structure of barium orthotitanate, Ba_2TiO_4, *Acta Crystallogr.*, 1961, **14**, 875, DOI: 10.1107/S0365110X61002527.

55 J. R. Günter and G. B. Jameson, Orthorhombic barium orthotitanate, α'-Ba_2TiO_4, *Acta Crystallogr.*, 1984, **C40**, 207–210, DOI: 10.1107/S0108270184003619.

56 F. Farges, G. E. Brown Jr and J. J. Rehr, Coordination chemistry of Ti(IV) in silicate glasses and melts: I. XAFS study of titanium coordination in oxide model compounds, *Geochim. Cosmochim. Acta*, 1996, **60**(16), 3023–3038, DOI: 10.1016/0016-7037(96)00144-5.

57 Z. Galazka, R. Uecker, K. Irmscher, M. Albrecht, D. Klimm, M. Pietsch, M. Brützam, R. Bertram, S. Ganschow and R. Fornari, Czochralski growth and characterization of β-Ga_2O_3 single crystals, *Cryst. Res. Technol.*, 2010, **45**, 1229, DOI: 10.1002/crat.201000341.

58 V. Kochurikhin, K. Kamada, K. J. Kim, M. Ivanov, L. Gushchina, Y. Shoji, M. Yoshino and A. Yoshikawa, Czochralski growth of 4-inch diameter Ce:$Gd_3Al_2Ga_3O_{12}$ single crystals for scintillator applications, *J. Cryst. Growth*, 2020, **531**, 125384, DOI: 10.1016/j.jcrysgro.2019.125384.

59 A. Ikesue and Y. L. Aung, Synthesis and performance of advanced ceramic lasers, *J. Am. Ceram. Soc.*, 2006, **89**(6), 1936–1944, DOI: 10.1111/j.1551-2916.2006.01043.x.

60 Q. Wei, S. Sun, F. Yuan, Y. Huang, L. Zhang, W. Chen and Z. Lin, A novel solid-solution garnet Yb:YAG-MnASG with enhanced spectral properties, *J. Alloys Compd.*, 2019, **786**, 77e83, DOI: 10.1016/j.jallcom.2019.01.308.

61 (*a*) CCDC 2448685: Experimental Crystal Structure Determination, 2025, DOI: 10.25505/fiz.icsd.cc2n61vs; (*b*) CCDC 2448696: Experimental Crystal Structure Determination, 2025, DOI: 10.25505/fiz.icsd.cc2n6265; (*c*) CCDC 2448697: Experimental Crystal Structure Determination, 2025, DOI: 10.25505/fiz.icsd.cc2n6276.